A real time Monte Carlo simulation of thin film nucleation in localized-laser chemical vapor deposition

Cite as: Journal of Applied Physics **64**, 4920 (1988); https://doi.org/10.1063/1.342442
Submitted: 14 March 1988 • Accepted: 13 July 1988 • Published Online: 30 September 1998

David E. Kotecki and Irving P. Herman

A real time Monte Carlo simulation of thin film nucleation in localized-laser chemical vapor deposition

David E. Kotecki[a]
Physics Department, Lawrence Livermore National Laboratory, Livermore, California 94550 and Department of Applied Science, University of California, Davis/Livermore, California 94550
Irving P. Herman
Department of Applied Physics, Columbia University, New York, New York 10027

(Received 14 March 1988; accepted for publication 13 July 1988)

A real time Monte Carlo simulation is used to model the nucleation and initial stages of thin film growth during localized-laser chemical vapor deposition (LLCVD). This model includes the effects of laser–substrate heating, heterogeneous pyrolytic decomposition of parent molecules on the laser-heated region of the surface, and adatom migration and desorption dynamics. The amount of material deposited as a function of time is obtained over a surface area of 150×150 Å for various values of the substrate temperature, parent gas pressure, and adsorbate–substrate binding energy. Additional information is obtained about the cluster density, and the role of surface defects and two-atom cluster dynamics on the initial growth rate. The deposition of silicon by heterogeneous pyrolytic decomposition of silane (SiH_4) is used as a base case for the simulation. Predictions of the initial thin film morphology and its temporal evolution during static laser heating of micron-dimensional regions of the surface are presented. Simulation results indicate that for a given silane pressure and adsorbate–substrate binding energy, there is a critical temperature T_c such that for laser-induced peak temperatures $T_p < T_c$, nucleation initiates at the center of the laser-heated region, while for $T_p > T_c$, nucleation occurs initially in an annulus region centered with respect to the incident laser irradiation. The inclusion of two-atom cluster dynamics in the simulation is shown to increase the value of T_c and alter the initial morphology for low adsorbate–substrate binding energies. The simulation results are extended to scanning LLCVD to predict the maximum scan speed at which nucleation will occur.

I. INTRODUCTION

Interest in localized-laser chemical vapor deposition (LLCVD) to produce discretionary, micron-dimensional thin films continues to expand.[1] During LLCVD, a substrate surface is initially in equilibrium with a static gas of parent molecules which contains the atom to be deposited. A focused laser produces a micron-dimensional heated region at the substrate surface. Parent molecules incident onto this localized reaction zone thermally dissociate into the deposit atom, plus a volatile product which eventually leaves the surface. In contrast to conventional large-area deposition processes, deposit atoms are laterally confined to this micron-dimensional laser-heated region. Scanning the laser with respect to the surface allows the thin film to be patterned across the substrate surface. Research on these direct-write techniques has been motivated by their potential application as single-step, mask-free alternatives in microelectronic processing.[2-5]

The process of nonepitaxial, three-dimensional island, thin film growth can be separated into three distinct stages: the nucleation phase, where a supersaturated concentration of adatoms combine to form critical nuclei which have a greater probability of growing than decaying; a coalescence stage, where critical nuclei grow together producing a contiguous thin film of material; and a continued growth stage, where material is deposited onto the already deposited film.

Understanding the dynamics associated with nucleation and the initial stages of thin film growth is important for controlling thin film properties. For example, thin film morphology and internal structure, such as whether a thin film of material is crystalline, polycrystalline or amorphous, are determined predominantly by the nucleation and early growth stages. The nucleation phase of thin film growth may also be the rate limiting step in deposition. Bloem and Claassen[6] reported this to be the case for the chemical vapor deposition (CVD) of silicon from silane (SiH_4) onto weakly binding substrates such as silicon dioxide (SiO_2) and silicon nitride (Si_xN_y). Finally, the first few monolayers of thin film atoms control both the interface properties of the thin film–substrate system, and the adhesion of the thin film to the substrate surface.

Because of the importance of this initial deposition step, the dynamics of nucleation has been the subject of numerous studies. Most attention has been given to nucleation during physical vapor deposition (PVD) of films by evaporation or sputtering, which has been addressed both experimentally and theoretically. These findings have been reviewed recently by Venables *et al.*[7] In contrast, less attention has been given to the nucleation and initial phase of thin film growth by the important technique of CVD. This is in part due to the additional features of multispecies gas-phase (homoge-

---

[a] Present address: IBM, General Technology Division, Hopewell Junction, NY 12533.

0021-8979/88/224920-23$02.40

neous) and surface (heterogeneous) chemistry in CVD, complications which are absent in PVD. Still, some significant studies have been conducted in this area. Of particular interest here is the work of Bloem and Claassen,[6,8-11] and Joyce and co-workers[12-14] on nucleation during CVD of silicon from silane (SiH_4). Under certain thin film growth conditions, the observed density of critical nuclei was $\leqslant 1\ \mu m^{-2}$. This result has interesting implications for thin film nucleation and growth during LLCVD where micron sized regions are formed.

The effects of nucleation have been shown to be important in LLCVD.[15,16] In these studies, several authors reported difficulty depositing material onto a bare substrate surface, but noticed that it became relatively easy to grow thin film microstructures onto either already nucleated areas of the surface, or starting from a previously written feature. For example, a focused laser can be scanned across a silicon substrate surface in the presence of silane (SiH_4) without producing a silicon deposit; but once the laser crosses a spot of deposited material, continued growth may commence without having to change laser power or the spot size. In general, this type of effect may be caused by changes in the optical or thermal properties of the deposited microstructure, but evidence exists that a nucleation effect is also partly responsible.

In an investigation by Tsao and Ehrlich,[17] laser processing was used to form the nucleation layer, and selected area deposition was then continued by thermal growth. They also discussed the importance of nucleation barriers for area-selective growth in these experiments.[18] Nucleation experiments on silicon deposition from $SiCl_4$ on silicon by LLCVD were conducted by Baranauskas *et al.*,[19] who identified three different regimes of initial growth. The initial silicon morphology was shown to be dependent upon the nucleation characteristics. A ~3-mm-diam spot size was used in these experiments, which is much larger than the micron dimensions considered here.

Previous models of LLCVD have concentrated on the post-nucleation growth phase. For example, a model of Ni deposition from $Ni(CO)_4$ by LLCVD was reported by Herman *et al.*[20] that included the effects of laser heating, reactant and product gas transport, and surface reactivity. Allen *et al.*[21] reported a model of Ni deposition during LLCVD which also took into account the change in optical properties of the material system caused by the growth of the thin film. Skouby and Jensen[22] investigated the resulting deposit morphology using a continuum model which took into account heterogeneous decomposition chemistry, gas transport, and laser–substrate and parent gas heating. Other features of modeling growth in LLCVD have been addressed by Tsao and Ehrlich,[18] Petzoldt *et al.*,[23] Moylan *et al.*,[24] and Kodas *et al.*[25]

The purpose of this investigation is to gain insight and understanding into some of the dynamical processes associated with the nucleation and initial stages of thin film growth during LLCVD. This is the first such model of nucleation effects during LLCVD. A Monte Carlo simulation is used to describe the dynamics of thin film deposition stochastically.

We previously reported on some aspects of nucleation during PVD[26] in which the duration and statistical uncertainty of the incubation period were shown to influence strongly the initial growth characteristics for deposition onto weakly binding surfaces. In the present paper, the Monte Carlo nucleation model used in that study is modified to include heterogeneous decomposition of reactant molecules and is used to examine some features of the initial thin film morphology expected during LLCVD.[27] As a specific example, the deposition of silicon onto strongly binding surfaces such as Si, and weakly binding surfaces such as SiO_2 and Si_xN_y, by heterogeneous decomposition of silane is simulated as a base case for our approach. In general, the model itself is applicable to other material systems.

In Sec. II, a seven-step model of LLCVD is presented. Specific features of this model such as laser heating, gas transport of reactants and products, and decomposition of reactant parent molecules are discussed. Details of the Monte Carlo simulation of nucleation are provided in Sec. III. The treatment of two-atom cluster migrations and desorptions, and the modeling of surface defects are also described. Results of the simulation of silicon nucleation from heterogeneous decomposition of SiH_4 on uniformly heated substrates are presented in Sec. IV. The connection between the simulation results and LLCVD is made in Sec. V, and the conclusions of this study are given in Sec. VI.

II. LOCALIZED-LASER CHEMICAL VAPOR DEPOSITION

A. Overview

In conventional CVD reactors, the sample susceptor and sometimes the walls of the reactor are resistively or inductively heated as parent gas along with a buffer gas are flowed through the reactor. Parent gas molecules dissociate either homogeneously or heterogeneously into the deposit atom plus volatile products producing a thin film of the deposit material onto the substrate surface. Modeling the flow and gas concentrations for a typical planar reactor geometry has been investigated by Coltrin *et al.*[28,29] In conventional CVD reactors, the total pressure is ~1 atm. Diffusion of parent gas molecules and gas products influences deposition greatly, and homogeneous gas phase dissociation of hot parent molecules usually dominates the chemical kinetics. In low pressure chemical vapor deposition (LPCVD) reactors, carrier gases are usually not used and the total gas pressure is generally $\leqslant 1.0$ Torr. At these reduced pressures, the rate limiting step in the deposition process shifts from the rate of diffusion of gaseous species between the bulk of the gas and the surface, to the rate of reactant parent molecule decomposition. Due to the surface controlled reaction rate, greater uniformity of large area thin film materials can be obtained than at higher pressures.

During LLCVD, the basic chemical reactions of large area CVD and LPCVD are combined with localized laser heating. The physical conditions in LLCVD differ considerably from those in conventional large area CVD and LPCVD. Light from a focused laser is absorbed by the substrate material creating a localized reaction zone with temperature rises of 100–1500 K over a spatial dimension of

$\sim 1.0\ \mu$m. Diffusion of reactant gas molecules to this point-like reaction zone is three dimensional, and the rate of impingement of parent molecules can be significantly greater than that occurring during the one-dimensional diffusion in large area CVD. Also, since the decomposition of parent molecules is localized to a micron-dimensional region, higher peak surface temperatures may be used in LLCVD than in large area CVD before homogeneous gas phase decomposition induces unwanted conglomerations of deposit atoms in the gas. In fact, successful deposition of silicon and nickel on silicon substrates by LLCVD with peak surface temperatures exceeding the substrate melting temperature has been reported.[30] Because of the increased rate of impingement of parent molecules and the higher surface temperatures, maximum vertical deposition rates in LLCVD are significantly faster than those in other thin film deposition processes. For example, vertical growth rates of 10^8 Å/s have been reported for the deposition of silicon from silane mixtures during LLCVD.[30] This can be compared to maximum deposition rates of 10^3 Å/s for large area CVD, 10^2 Å/s for sputtering and evaporation, and 10^1 Å/s for molecular beam epitaxy.

The physics of film growth by LLCVD can be described by the following seven-step model:

(1) Interaction of the laser photons with the surface to produce a locally heated reaction zone and possibly to modify the surface reactivity (e.g., through increased electron-hole pair density or direct photon induced desorption of adsorbate atoms) (Sec. II B).

(2) Transport of the reactant gas to the laser-heated region of the substrate surface (Sec. II C).

(3) Adsorption of the reactant molecule on the substrate surface (Sec. II D).

(4) Decomposition of the reactant gas on the laser-heated region of the surface or in the gas phase to produce deposit atoms (Sec. II D).

(5) Interaction of the adsorbed atoms to form a thin deposit of material (Secs. III–V). (a) Nucleation of adsorbed atoms, in which a supersaturated concentration of adatoms combine to form critical nuclei that have a greater probability of growing than decaying; (b) Coalescence of the critical nuclei; (c) Deposition of material onto already deposited material.

(6) Desorption of volatile products from the laser-heated surface (Sec. II D).

(7) Transport of the product gas away from the substrate surface (Sec. II C).

These seven steps are not sequential but occur simultaneously during deposition.

This study concentrates on step 5 in the above sequence. All other steps are considered in sufficient detail to model the nucleation process in LLCVD properly.

B. Laser-induced temperature distribution

Proper consideration of the laser-induced surface temperature profile is necessary in the study of nucleation and growth of thin films by LLCVD. In this study a laser source with a constant intensity is assumed to irradiate the surface for a characteristic time τ_{dwell}. A detailed laser-induced temperature distribution is obtained from a finite difference solution of the heat diffusion equation.

Only a steady-state temperature profile need be considered as long as the characteristic time τ_t for the substrate to reach a steady-state temperature is short compared to the laser duration τ_{dwell}, and if the growth of the thin film does not affect the optical properties (by a change in reflectivity or absorption) or thermal properties (by a change in thermal conductivity) of the thin film–substrate system. During LLCVD, the duration of the laser pulse τ_{dwell} is generally $\geqslant 100\ \mu$s. (When the laser beam is scanned across a surface at velocity v, the duration of the laser dwell time $\tau_{\text{dwell}} \sim S/v$, where S is the FWHM laser intensity at the surface.) The characteristic time needed for a material system to reach a steady-state temperature distribution τ_t is dominated by thermal transport and is approximated by $\tau_t \sim S^2/D$, where D is the thermal diffusivity. Even for highly insulating solids, the thermal diffusivity $D \geqslant 10^{-3}$ cm^2/s. Thus for $S = 1\ \mu$m, $\tau_t < 10\ \mu$s, therefore $\tau_t < \tau_{\text{dwell}}$, validating a steady-state approximation for laser heating of a substrate. Since the nucleation and early stages of thin film growth will only perturb the thermal and optical properties of the substrate slightly, the steady-state temperature approximation is assumed here.

An analytical solution to the steady-state thermal diffusion equation for conditions encountered during laser heating of substrates has been obtained by Lax,[31] Moody and Hendel,[32] and others. These solutions are not of simple form, and are not sufficiently general in taking into account the temperature dependence of the thermal and optical properties of the materials. Here, the thermal diffusion equation is solved computationally by the Gauss Seidel finite difference method to obtain the temperature profile.

The material system considered consists of a silicon substrate with an optional thin film (< 1000 Å) coating of either silicon dioxide (SiO_2) or silicon nitride (Si_xN_y) which is surrounded by a gas such as air, a system of particular interest in microelectronics. The silicon is characterized by a temperature-dependent thermal conductivity $K_{\text{Si}}(T)$, absorption coefficient $\alpha_{\text{Si}}(T)$, and index of refraction $n_{\text{Si}}(T)$. The optional thin film of SiO_2 or Si_xN_y is characterized by a constant thermal conductivity K_{film} and index of refraction n_{film}. Details of the materials properties and the solution of the thermal diffusion equation are given in Appendix A.

Figure 1 shows the temperature distribution computed for a Gaussian laser profile at a wavelength of 514.5 nm, with a 2.5-μm FWHM incident onto a 500-Å thin film of SiO_2 on a silicon substrate for the power levels between 200 and 450 mW. For this particular material system, it is noted that the width of the temperature distribution (FWHM) is approximately the same as the laser intensity profile. At peak temperatures approaching the melting temperature of the silicon substrate (1690 K), the thermal distribution is slightly narrower than the laser intensity profile, while at low power levels and low peak temperatures, the thermal distribution is slightly broader than the laser intensity profile. Thin film growth takes place only on this locally heated region of the substrate surface.

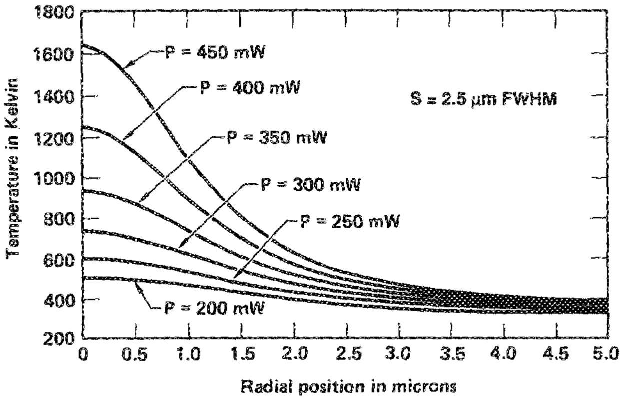

FIG. 1. Computed thermal distribution produced by a Gaussian laser profile for 514.5 nm, with a 2.5 μm FWHM and power P incident onto a 50-nm thin film of SiO_2 on a silicon substrate.

C. Gas transport

The general problem of gas transport during LLCVD is quite complex. Consider an LLCVD reactor in which a static pressure of parent gas molecules is initially in equilibrium with the substrate surface. Transport of parent molecules from the bulk of the gas to the laser-heated region of the surface, and the transport of parent molecules and dissociation products from the surface to the bulk of the gas, must be considered.

The character of the gas transport depends critically on the Knudsen number $K_n = l/S$, where l is the molecular mean free path.[33] When $K_n \ll 1$, gas collisions strongly influence the transport and the gas can be treated as a multicomponent fluid. Since most CVD chemical reactions liberate at least as many species as they absorb, outward convection of high velocity gas species is important. Molecules entering the reaction zone must travel against this outward convection induced by a high velocity product gas, causing deposition to be limited more by the supply of parent molecules than by the removal of products. For the case in which there is no net generation of molecules, gas convection becomes relatively weak and the transport of parent molecules and products is a diffusion-limited process. Herman *et al.*[20] have analyzed this regime for the case of constant gas diffusion coefficients (D_g) and found that the transport rates scale as D_g/S, a considerably lower velocity than the sonic velocity.

The other important limiting case of gas transport in LLCVD is the molecular flow regime which occurs at high Knudsen numbers, $K_n \gg 1$. In this case, the rate at which gas parent molecules are incident onto the laser-heated region of the surface is equal to the equilibrium flux of molecules at the surface, which is $nv_g/4$ for an ideal noninteracting gas, where n is the density and v_g is the average velocity. The mean number of parent molecules incident onto the surface per square centimeter per second R_P is given by

$$R_P = 3.51 \times 10^{22}\, P/(MT_g)^{1/2}, \tag{1}$$

where R_P has the units of $cm^{-2}\,s^{-1}$, P is the pressure in Torr, M is the molecular mass, and T_g is the temperature of the gas in Kelvin. Consider SiH_4 gas (300 K) incident onto a model surface with a simple cubic structure containing 1.36×10^{15} atomic sites/cm^2 (the average planar atomic density of silicon). Equation (1) reduces to

$$R_{SiH_4} = 2.63 \times 10^5\, P_{SiH_4}, \tag{2}$$

where R_{SiH_4} is now the rate of impingement in units of (atomic site)$^{-1}$ s^{-1}, and P_{SiH_4} is the silane pressure in Torr. For micron-dimensional laser-heated reaction zones, this condition is valid for reactant gas pressures < 10 Torr.

Since the present study emphasizes the nucleation aspects of thin film growth, only the low pressure regime of gas transport is considered in order to avoid the added complication of gas phase diffusion in the high pressure regimes. For the nucleation simulations, Eq. (2) is used to estimate the flux of parent molecules incident per unit area per second onto all surfaces, regardless of the actual lattice spacing. One additional consequence of this low pressure assumption is that the molecular dissociation chemistry can be simplified in this regime. This is discussed in the following section.

D. Molecular dissociation chemistry

1. General considerations

The chemistry occurring during large area CVD and LPCVD, and also during LLCVD may involve both homogeneous and heterogeneous decomposition mechanisms. The computed temperature profile in one atmosphere of ideal gas directly above the center of the laser irradiation region during typical LLCVD conditions is shown in Fig. 2. As in Fig. 1, a Gaussian laser profile at a wavelength of 514.5 nm, with a 2.5-μm FWHM diameter is incident onto 50 nm of SiO_2 on a silicon substrate. The temperature calculation takes into account only conductive heat flow and is discussed in Appendix A. As can be seen, the gas temperature drops off rapidly in the gas, but even at a distance of 1 μm above the surface, the temperature can still be sufficiently high to allow homogeneous decomposition of the parent molecules.

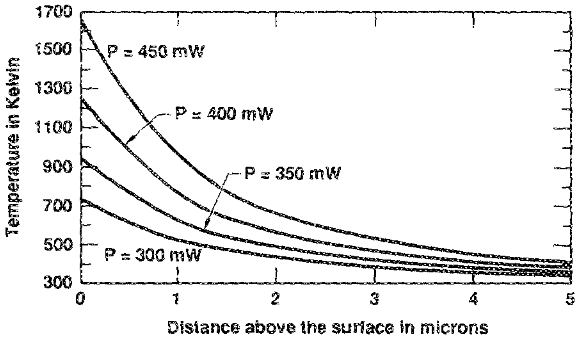

FIG. 2. Computed thermal profile in one atmosphere of ideal gas as a function of distance directly above the center of the laser-heated region of the surface for the same conditions as in Fig. 1.

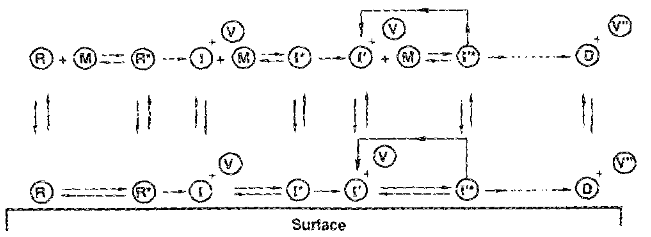

FIG. 3. Schematic representation of possible molecular dissociation channels for reactant molecule R, intermediate radicals $I, \acute{I},\ldots,\acute{\acute{I}}$, volatile products $V, \acute{V},\ldots,\acute{\acute{V}}$, and deposit atom D.

During the decomposition process, many intermediate species may be formed and contribute to the decomposition and the deposition process. A simplified general description of homogeneous and heterogeneous decomposition is shown in Fig. 3. Consider a reactant molecule R which contains only a single deposit atom D. The reactant molecule R may become activated upon collision with another gas molecule M or with the surface. The activated molecule R * then decomposes into an intermediate radical I which contains the deposit atom D and a volatile product V. This intermediate I can then become activated either upon a collision with another gas molecule M or the surface and further decompose into another intermediate $\acute{I}$ plus another volatile $\acute{V}$. This chain continues until an intermediate decomposes into the deposit atom D plus any remaining volatile products $\acute{\acute{V}}$. Transfer of the reactant molecule R, intermediates $I, \acute{I},\ldots,\acute{\acute{I}}$, and the deposit atom D between the gas and the surface can also take place and the migration of the various species on the substrate surface could also affect the nucleation and initial growth characteristics. Intermediate radicals, volatiles, and reactant molecules can also react with one another producing more complex compounds which either dissociate, or possibly take up adsorption sites on the surface; this complication is not treated in this model.

Two important features unique to low pressure (< 10 Torr) LLCVD allow a simplification of the general decomposition chemistry. First, at low reactant gas pressures, the mean free path in the gas phase is equal to or larger than the extent of the localized reaction zone. Therefore a gas phase reactant molecule or intermediate which is activated by a collision with the surface or another gas molecule will most likely leave the reaction zone without colliding with another molecule or decomposing further. Intermediates generated in the gas phase or on the surface will leave the pointlike reaction zone at much greater rates than they will be supplied from the bulk of the gas. Second, the decomposition energy for most molecules is much greater than the average energy associated with the laser modified surface temperature. Since the reaction zone is localized in a micron-dimensional region, the reactant molecule needs to undergo many collisions to be activated to the decomposition energy. During low pressure LLCVD a sufficiently high gas phase temperature will not be obtained. Thus at low pressures, the decomposition mechanism in LLCVD is entirely heterogeneous and the effects of homogeneous decomposition may be ignored.

2. Heterogeneous decomposition

Table I delineates the possible steps of heterogeneous decomposition. In this surface-reaction mechanism, the reactant R adsorbs onto the surface (1a). The reactant molecule can then desorb from the surface (2a), migrate on the surface (2b), dissociate into an intermediate plus a volatile (2c), or dissociate directly to the deposit atom plus a volatile (2d). Intermediates $I, \acute{I},\ldots,\acute{\acute{I}}$ can desorb from the surface (3a), migrate on the surface (3b), dissociate into another deposit atom bearing species plus a volatile (3c), dissociate into a deposit atom plus a volatile product (3d), or interact with another intermediate or volatile M forming a different intermediate and possible volatile (3e). Volatiles $V, \acute{V},\ldots,\acute{\acute{V}}$ can undergo these same processes. The dynamics of the adatoms themselves D are described by desorption (5a), surface migration (5b), and nucleus incorporation (5c). In most cases, the decomposition chemistry is not completely known. Reactions (1b) and (1c) represent examples of net

TABLE I. General model for heterogeneous decomposition of a reactant molecule R into intermediates $I, \acute{I}, \acute{\acute{I}}$, volatiles $V, \acute{V}, \acute{\acute{V}}$, and the deposit atom D.

$R(g)$	$\to R(s_i)$	(1a)	$R(s_i)$	$\to R(g)$	(2a)
	$\to I(s_i) + V(g)$	(1b)		$\to R(s_j)$	(2b)
	$\to D(s_i) + V(g)$	(1c)		$\to I(s_i) + V(s_j)$	(2c)
				$\to D(s_i) + V(s_j)$	(2d)
$I(s_i)$	$\to I(g)$	(3a)	$V(s_i)$	$\to V(g)$	(4a)
	$\to I(s_j)$	(3b)		$\to V(s_j)$	(4b)
	$\to \acute{I}(s_i) + \acute{V}(s_j)$	(3c)		$\to \acute{V}(s_j) + \acute{\acute{V}}$	(4c)
$I + M(s_i)$	$\to D(s_i) + V(s_j)$	(3d)		$\to \acute{\acute{V}}(s_i)$	(4d)
	$\to \acute{I}(s_i) + \acute{\acute{V}}(s_j)$	(3e)	$V + \acute{V}(s_i)$	$\to$ (4a)...(4d)	(4e)
$\acute{I}, \acute{\acute{I}}$	$\to$ (3a)...(3e)	(3f)	$\acute{V}, \acute{\acute{V}}$		
$D(s_i)$	$\to D(g)$	(5a)			
	$\to D(s_j)$	(5b)			
	$\to$ nucleus incorporation	(5c)			

reactions, combining elements of reactions (2a)–(4e), which may have to be used when reaction details are unavailable.

3. Silane pyrolysis

As a base case for the nucleation calculations, the deposition of silicon from silane (SiH_4) is considered. Though silane pyrolysis has been extensively studied, the current state of understanding is still incomplete. During conventional CVD, molecular dissociation of a silane molecule can occur homogeneously in the gas phase, as well as heterogeneously on a heated surface. At pressures above ~100 Torr, the dominant decomposition path initiates via the homogeneous pressure-dependent unimolecular reaction[34,35]

$$SiH_4(\text{gas}) \rightarrow SiH_2(\text{gas}) + H_2(\text{gas}) \tag{3}$$

which is followed by the surface controlled reaction

$$SiH_2(\text{gas}) \rightarrow SiH_2(\text{adsorbed}) \rightarrow Si + H_2(\text{gas}). \tag{4}$$

The activation energy for the initial decomposition [Eq. (3)] is reported to $\simeq 52$ kcal/mol,[36,37] while that required for the decomposition of the silylene (SiH_2) radical is estimated by Coltrin *et al.*[28] to $= 2$ kcal/mol. During high pressure CVD, the diffusion of the silylene radical to the surface is considered the rate limiting step of the deposition process. The growth rate is observed to be independent of the hydrogen pressure[38] and thus adsorbed hydrogen does not inhibit the growth and can be ignored.

At low pressures, the reaction may be surface initiated.[37,39] Molecular-beam studies of silane cracking provide accurate rates of heterogeneous decomposition. Farrow[40] investigated the kinetics of silane pyrolysis on a silicon (111) surface mass spectrometrically during molecular-beam sampling for the silane pressures $P_{SiH_4} = 1\times10^{-5}$–0.4 Torr and a silicon surface temperature $T = 300$–1473 K. The silicon growth rate was found to be linear with pressure indicating a first-order decomposition reaction and the proposed silane decomposition mechanism was

$$SiH_4(\text{gas}) \rightarrow SiH_4(\text{adsorbed}) \rightarrow Si + 2H_2. \tag{5}$$

The activation energy for decomposition was measured to be 17 ± 2 kcal/mol^{-1} and the surface reaction efficiency Θ was determined to be

$$\Theta(T) = 5.45 e^{-1.7\times10^4/\bar{R}T}, \tag{6}$$

where $\bar{R}$ is the molar gas constant (1.98 cal mol^{-1} deg^{-1}). No significant (<5%) difference between silane decomposition on a silicon (111) surface or a polycrystalline surface at the same temperature was observed. Henderson,[41] Joyce *et al.*,[12,13,14] and Farnaam and Olander[42] have also measured the thermal cracking of silane on a silicon surface, and have reported decomposition activation energies of 20 ± 5, 18.7 ± 2, and 17 kcal/mol^{-1}, respectively. Recently, Buss *et al.*[43] measured the reactive sticking coefficient (probability that a silane molecule impinging on the surface leaves a silicon atom on the surface) for silicon formation from silane on polycrystalline silicon. For pressures $\lesssim 0.3$ Torr and at high temperatures $T \sim 1300$ K, they found the reactive sticking coefficient to be independent of pressure. At lower temperatures, the reactive sticking coefficient was found to decrease monotonically with increasing pressure.

The subject of atomic hydrogen formation was addressed by Farnaam and Olander[42] using mixed molecular beams of SiH_4 and SiD_4. Mass spectrometric analysis indicated no presence of HD molecules, ruling out the production of atomic hydrogen in the surface reaction mechanism and the possible poisoning of nucleation sites by hydrogen atoms. Also, the residence time of SiH_4 on a silicon surface was reported to be $< 5\,\mu$s, ruling out the desorption of silane [(2a) in Table I] as a rate limiting step in the growth process.

Deposition of Si from SiH_4 onto surfaces of SiO_2 was studied by Seto[44] and Bloem and Claassen.[6,8,10] The work of Seto showed that H_2 produced by the dissociation of SiH_4 has no effect on the silicon growth rate. A three-step mechanism of SiH_4 decomposition consistent with that reported by Farrow was found. The decomposition rate of silane on surfaces of SiO_2 was not measured.

In this study, the rate of silicon adatom production from silane decomposition during LLCVD is modeled by combining the rate of silane incidence given by Eq. (2), times the reaction efficiency of Farrow, Eq. (6) thus producing

$$R_{Si} = R_{SiH_4} \times \Theta(T) = 1.43\times10^6 e^{-1.7\times10^4/\bar{R}T} P_{SiH_4}, \tag{7}$$

where $T = T(\mathbf{r})$ is a function of spatial position on the laser-heated surface region. In this simplified model, which corresponds to the net reaction (1c) in Table I, the silylene radical and molecular hydrogen on the surface are assumed to affect the nucleation and early growth dynamics negligibly. Though Eq. (6) was obtained only for silicon surfaces and for temperatures only up to 1473 K, it and Eq. (7) are assumed to be valid for all model surfaces and to the melting temperature of silicon, 1690 K. Any possible laser-induced modifications to the surface reactivity by photon-adsorbate interactions or electron-hole pair creation are ignored here.

III. NUCLEATION MODEL

A. Introduction

Nucleation dynamics during low pressure LLCVD are investigated via a real time Monte Carlo simulation. Previous Monte Carlo models of nucleation have been reported by Abraham and White,[45] Ghaisas and Madhukar,[46] Gilmer and Broughton,[47] Kashchiev *et al.*,[48] Michaels *et al.*,[49] Outlaw and Heinbockel,[50] Van der Eerden *et al.*,[51] and Salik[52] among others. All of these simulations dealt with a system of PVD in which deposit atoms impinged directly onto the surface, as during deposition by evaporation or sputtering. In most cases, in order to fit the time scale of the simulation to real world conditions, a time scale factor was needed in these models to effectively accelerate the simulations to make them comparable to real deposition parameters.

The Monte Carlo simulation model considered here consists of a three-dimensional grid, which, for simplicity, is assumed to have simple cubic symmetry to represent the possible positions of deposit atoms. All simulations describe adatom dynamics in real time; no time scale factor is needed. The reactant molecule impingement rate, which is described by Eq. (2), relates the simulation to a real value of time. Silane is used as a base case to model the deposit adatom formation rate using Eq. (7), as described in Sec. II D 3. The interaction of deposit bearing intermediates and volatiles on the surface are not included in the present model, but the model could be extended to include such interactions.

The dynamics of each adatom for each step is determined by its surroundings, which consist of a subcube of 26 atoms; nine on the plane below the atom, nine on the plane above the atom, and eight on the same plane as the atom. Each atom is allowed to move into any of the 26 sites of the subcube which is not already occupied by an atom. Thus, interstitial vacancies within the film are allowed to form. Random boundary conditions are employed. That is, if an adatom migrates outside the lateral confines of the simulation grid, it is returned to the periphery at a randomly chosen site.

In some simulations, migration and desorption of two atom clusters of atoms are allowed. Due to the excessive amount of computer processing time required to calculate the probabilities of all possible two atom cluster migrations and desorptions, this feature was included only in one set of simulations as discussed below. Also, the effect of defect sites with a strong binding energy was investigated. All calculations were carried out on either a Cray-1 or Cray-XMP computer and the amount of time to produce one-tenth of a monolayer took between 15–200 min depending upon the conditions simulated.

B. Adatom surface dynamics

In addition to the atomic formation rate, two other important physical processes influence the nucleation process: adatom desorption and adatom migration. These correspond to reactions (5a) and (5b) of Table I, respectively. During the nucleation process of thin film growth, there is the constant competition between the generation of new nuclei by adatom migration and capture, and the loss of adatoms from the growing surface by adatom desorption. It is this dynamical condition between adatom migration and desorption which determines the rate of initial thin film growth and the density of critical nuclei.

The mean residence time τ_d that a single adsorbed atom spends on the substrate surface before desorbing is given by[53]

$$\tau_d = \nu_0^{-1} e^{E_d/kT}, \tag{8}$$

where E_d is the average adsorption energy, assumed here to be independent of position and temperature on the substrate, and ν_0 is the rate constant for desorption which is taken to $= 10^{12}\ \mathrm{s}^{-1}$, and is also assumed to be independent of temperature.

The mean time between migrations across adjacent sites on the substrate is given by[53]

$$\tau_m = \nu_1^{-1} e^{E_m/kT}, \tag{9}$$

where E_m is the average activation energy required for a migration of a single adatom on the substrate to an adjacent site and is assumed to be independent of position and temperature; ν_1 is the rate constant for migrations and is taken to be equal to $\nu_0 = 10^{12}\ \mathrm{s}^{-1}$.

Considering purely random walk behavior, the average displacement of an adatom from an initial position is equal to the average step distance in all directions times the square root of the number of steps. Thus the average distance an adatom migrates before desorbing is given by

$$\Lambda = \left(\frac{\tau_d}{\tau_m}\right)^{1/2} d = e^{(E_d - E_m)/2kT} d, \tag{10}$$

where d is the average distance between atomic sites on the surface. The parameter Λ is used to determine the simulation grid size needed to describe nucleation adequately. For the adatom dynamics to be represented correctly, the linear dimension of the simulation grid must be $> \Lambda$.

Another important quantity in adatom surface dynamics is the characteristic time between adatom surface events, where an event corresponds to either an adatom migration or desorption. This characteristic time τ_c is given by

$$\tau_c = \left(\frac{1}{\tau_m} + \frac{1}{\tau_d}\right)^{-1} = \nu_0^{-1}\left(e^{-E_m/kT} + e^{-E_d/kT}\right)^{-1} \tag{11}$$

and represents the time scale of adatom surface dynamics. The values of these parameters are given in Sec. IV A, where the simulated conditions are reviewed.

C. Adatom binding energies and migration barrier heights

An empirical bond-breaking model is used to determine the amount of energy which must be supplied for an adatom to move from one site to another. The lowest layer of the grid consists of the surface atoms which are stationary and do not change. Even though amorphous surfaces, such as those of SiO_2 and Si_xN_y, are not periodic in nature and should be characterized by a distribution of binding sites,[54] a single average adatom/surface-atom binding strength is used here to characterize the adsorbate/surface interaction.

The binding energy $E_{a\text{-}s}$ is defined as the bond strength of a single adatom to a nearest-neighbor surface atom, while the binding energy $E_{a\text{-}a}$ is the bond strength between two nearest-neighbor adatoms. The bond strengths of the next-nearest-neighbor and next-next-nearest-neighbor atoms of the subcube are given by the nearest-neighbor bond energy $E_{a\text{-}s}$ or $E_{a\text{-}a}$ times a relative bond strength factor bs_2, and bs_3, respectively. It is assumed that all bond strengths are additive.

Since nucleation is a dynamical process, the salient physics is modeled by simulating the migrations and desorptions of single adatoms (and possibly small clusters of adatoms) such that the correct statistically averaged number of migrations and desorptions given by Eqs. (8) and (9) are maintained. An exact knowledge of the interatomic potential is not essential. For the results presented here, the Van der Waals attraction of the Leonard Jones 6–12 interatomic potential $V(r) = E_{a\text{-}x}(r/d)^{-6}$ is used where x is either a or s for an adsorbed atom or substrate bond, respectively, and d is the nearest-neighbor distance. Changing the power n in the interatomic potential $V(r) \propto (r/d)^{-n}$ between 4 and 8 did not greatly affect the nucleation and initial growth results as long as the ratio of the migration energy E_m to the desorption energy E_d was held constant, and if the number of migrations between consecutive incident silane molecules Ψ, also remained fixed. For a Van der Waals attraction, the normalized bond strength factor for nearest-neighbor bonds bs_1 is 1, while bs_2 and bs_3 are 0.125, and 0.026, respectively.

The adatom being considered in any step of the simulation is always positioned at the center of the subcube. The energy barrier for a specific move E_p from the center of the subcube to any of the other 26 positions within the subcube (p), is obtained from the following rules:

(1) If the position p is already filled with an atom, the move is not allowed and the energy barrier $E_p = \infty$.

(2) If the position p is empty, the energy barrier E_p for a single move is determined by the bonds which are broken or weakened: (a) All bonds which are no longer part of the subcube of the atom after the move are considered broken. E_{p_b} is the sum of all broken bond energies,

$$E_{p_b} = \sum_{\text{broken bonds}} bs_i E_{a\text{-}x} , \tag{12}$$

where $i = 1, 2, 3$, and $x = s$ or a depending on whether the bond was with a surface atom or another adsorbed atom. (b) All bonds which are still part of the new subcube after the move but have become weaker ($bs_1 \rightarrow bs_2$ or $bs_2 \rightarrow bs_3$) and a nearest-neighbor bond strength which has stayed the same ($bs_1 \rightarrow bs_1$) are considered stretched bonds. The contribution to the activation energy is the initial bond strength times a factor f, where f is set to provide the desired ratio of migration energy to desorption energy for a single adatom adsorbed onto a bare substrate (see Sec. III D), and is an adjustable parameter in the model. E_{p_s} is the sum of all stretched bond energies,

$$E_{p_s} = \sum_{\text{stretched bonds}} bs_i E_{a\text{-}x} f . \tag{13}$$

(c) If the particular bond becomes stronger as a consequence of the move, it does not contribute to the total energy of the move. (d) The total barrier energy E_p for a specific move to position p is the sum of energies from broken and stretched bonds

$$E_p = E_{p_b} + E_{p_s} . \tag{14}$$

(3) If the adatom is no longer attached to any of the deposit or surface atoms after a migration (e.g., a migration straight up with no other atoms surrounding it) or if the adatom is attached to the thin film with a total binding energy $< E_{a\text{-}a}$, the atom is considered desorbed and no longer part of the thin film. Desorbed atoms do not reimpinge upon the surface, as is expected for a localized reaction zone.

In this model, there is no distinction between adatom migration and desorption since migrations and desorptions are treated equally. A desorption is just a migration to a position where the adatom is no longer on the surface and the total binding energy of the adatom is $< E_{a\text{-}a}$.

All 26 possible single adatom migration energy barriers can be summarized by eight distinct equations governing the migrations to a corner and an edge on each of the three planes, as well as a migration straight up and straight down. These barrier energies are summarized in Appendix B; migrations to the other sites can be obtained by an appropriate rotation of the subcube.

D. An adatom on a bare substrate

Consider an adatom formed onto a bare substrate. The energy barrier for a move to any of the nine positions in the plane above the adatom using the prescribed rules stated above is represented by

$$E_d = (1 + 4bs_2 + 4bs_3) E_{a\text{-}s} . \tag{15}$$

Since the adatom will no longer be attached to any other adatoms or the surface, the atom would be considered desorbed and E_d gives the proper desorption energy for an adatom on a bare surface.

To describe the migration of a single adatom on a bare surface, adatom migration on the plane above the substrate to the four corner positions along the diagonal and the four side positions in the direction parallel to an edge of the subcube need to be considered. A migration energy barrier to any of the four corner positions of the subcube E_{m_c} is given by

$$E_{m_c} = (f + 2bs_2 + 3bs_3) E_{a\text{-}s} \tag{16}$$

and for migration to any of the four side positions of a subcube E_{m_s} is given by

$$E_{m_s} = [f + (1 + 2f) bs_2 + 2bs_3] E_{a\text{-}s} . \tag{17}$$

Since the nine positions of the subcube below the plane of the adatom are filled, movement into these positions is not allowed.

For a single adatom on a bare substrate, there are nine possible positions for adatom desorption, and only eight possible positions for adatom surface migration, leading to a statistical weight of $\frac{8}{9}$ in the ratio of the number of migrations to the number of desorptions per second. [This factor, which is of order unity, is an anomaly inherent in the formulation of the model and does not produce an unphysical effect in the model. Also, this factor of $\frac{8}{9}$ could be incorporated into the ratio of the preexponentials ν_0^{-1} and ν_1^{-1} in Eqs. (8) and (9).]

The average migration energy E_m is taken as the average of the migration energies to a corner and a side position and is given by $E_m = (E_{m_c} + E_{m_s})/2$. The factor f is adjusted to provide the desired ratio of migration energy to desorption energy for a single adatom on a bare substrate surface and can be determined once an interaction potential is specified. Using Eqs. (15)–(17) and a Van der Waals interaction, $f = 0.5$ will give $E_m = 0.51\ E_d$, and will produce the near equality $E_m \sim E_{m_c} \sim E_{m_s}$.

A single adatom on a bare substrate will undergo a greater number of events (i.e., migrations + desorptions) per unit time than will adatoms on a surface with other adsorbed atoms since the additional binding of adatoms with other deposited atoms will hinder migration and desorption. Thus, the maximum number of adatom events Ψ occurring between the successive impingement of reactant molecules to a surface site occurs for a single adatom on a bare substrate and is given by

$$\Psi = \frac{1/R_{\mathrm{SiH}_4}}{\tau_c} = \frac{3.80 \times 10^6 (e^{-E_m/kT} + e^{-E_d/kT})}{P_{\mathrm{SiH}_4}} , \tag{18}$$

where R_{SiH_4} is the rate of SiH_4 molecules to the surface per second per site [Eq. (2)] and τ_c is the characteristic time of adatom surface event [Eq. (11)].

Since, in the model of silane decomposition, the incident reactant molecule either desorbs or decomposes directly into the deposit atom in a single step and interactions of intermediates and volatiles are ignored, the number of adatom surface events per incident reactant molecule can be formulated in terms of the rate of adatom generation as was done in Ref. 27. The number of adatom surface events per silicon adatom generation per site, $\Phi = \Psi/\Theta$ is then given by

$$\Phi = \frac{6.98\times 10^5 e^{1.7\times 10^4/\tilde{R}T}\left(e^{-E_m/kT} + e^{-E_d/kT}\right)}{P_{\mathrm{SiH}_4}} \tag{19}$$

using Eq. (6) for Θ.

The single adatom on a bare substrate provides a lower limit to an adatom migration or desorption energy barrier. In the model presented here, the maximum migration energy barrier occurs when the entire subcube is filled except for the position directly above the central adatom in which case,

$$E_p = E_d + 4(1 + bs_2)E_{a\text{-}a} . \tag{20}$$

For all intermediate cases, the more general prescription given in Appendix B is used to compute the energy barrier for all possible adatom events.

E. Dimer migrations and desorptions

The simulation also includes a provision to allow two-atom clusters of atoms (dimers) to migrate and desorb from the surface. The same formalism used for single atom migrations and desorptions is applied to the dimer pairs. An additional 130 equations similar to those in Appendix B are used to describe the migration of all possible dimer pairs. Only nearest-neighbor adatoms are considered dimer pairs. It requires 26 equations describing the possible moves for each of the dimer pair configurations: an atom attached to the north, south, east, west, or below the specified adatom.

The energy barriers representing a dimer move from one site to another site in this model were obtained by the same set of rules stated in Sec. III C. Due to the complexity and number of equations governing dimer movement, they are not presented here explicitly.

F. Evaluation of event probabilities

Once the energy barriers of all possible single adatom and dimer cluster (if included in the simulation run) movements are calculated, the probability P_p for each of the possible moves is obtained using a Boltzmann distribution,

$$P_p = e^{-E_p/kT}/q , \tag{21}$$

where E_p is the activation energy for a migration to a specific location p, and q is the normalization factor. This normalization factor is the maximum value of the sum of all the probabilities for a single adatom which is obtained from a single adatom on a bare surface and is given by

$$q = e^{-4E_{m_s} - 4E_{m_c} - 9E_d} , \tag{22}$$

where E_d is the desorption energy, E_{m_c} is the migration energy in the direction along the diagonal, and E_{m_s} is the migration energy in the direction parallel to an edge of the cubic lattice, which are given by Eqs. (15)–(17), respectively.

For an adatom on a bare substrate, $\Sigma_p P_p = 1$, while for a substrate covered with other adatoms $\Sigma_p P_p \leqslant 1$. To determine which, if any, adatom event takes place, the 26 possible probabilities P_p are calculated from Eq. (21). A random number P_R between 0 and 1 is generated. The smallest possible value of p^* such that $\Sigma_{p=1}^{p^*\leqslant 26} P_p \geqslant P_R$ determines the event P_{p^*} which takes place, and the surface is updated to reflect the change. However, if $\Sigma_{p=1}^{26} P_p < P_R$, then a null event occurs, and no migration or desorption takes place, thus leaving the surface unchanged.

G. Simulation procedure

The general sequence of events in the simulation for the example of silicon deposition from silane is as follows:

(1) Initial conditions and growth parameters including the pressure, binding energies, and temperature are established.

(2) Two random numbers are generated to establish a random position (x,y) on the grid and a reactant molecule is placed at the lowest unoccupied vertical position at location $(x,y,z_{\min})$. The molecule dissociates at that site with a probability of dissociation given by Θ in Eq. (6) or the molecule desorbs from the surface with a probability $1 - \Theta$.

(3) The "relaxation" process of adatom dynamics is simulated: (a) A random number selects a surface adatom. (b) Probabilities for all possible events (adatom migrations and desorptions, and when included two atom cluster migrations and desorptions) are computed using the energy barrier algorithm given in Appendix B and Eq. (21). (c) A random number is generated which determines which event, if any, takes place by comparing the random number to a normalized Boltzmann distribution as described in Sec. III F. (d) The grid representing the locations of atoms is updated to reflect the previous move.

(4) The relaxation process (step No. 3) is repeated until the average number of relaxations attempted per adsorbed atom equals Ψ/N, where Ψ is the number of adatom events between incident reactant molecules to each site on the surface given by Eq. (18), and N is the number of surface adsorption sites in the simulation grid. If a desorption took place during the previous relaxation step, the value of Ψ/N is updated by considering the average number relaxations per adatom up to that time.

(5) Step Nos. 2–4 are repeated until the desired surface coverage is obtained.

It should be noted that in this model the rate at which reactant molecules are incident and their rate of dissociation are completely deterministic. The stochastic nature of the rate of incidence is only taken into account by randomizing the positional distribution of incident reactant molecules. Also, the "relaxation" process (step No. 3) is stochastic.

H. Addition of nucleation sites

Nucleation sites, which could be caused by surface contaminants or surface defects, were added in some of the simulation runs. A simplified model of a nucleation site was used in which the nucleation site was represented by an infinite potential well placed at a specific location on the surface of the simulation grid. An adsorbed atom reaching this site becomes bound to the surface and has a zero probability of migrating or desorbing.

IV. SIMULATION RESULTS OF NUCLEATION

A. Overview of conditions simulated

Simulation conditions were chosen to represent those of low pressure LLCVD of silicon from SiH_4 onto strongly binding substrates such as silicon, and weakly binding substrates such as SiO_2 and $Si_x N_y$. The molecular dissociation rate of silane described in Sec. II D 3 was used exclusively to determine the adatom formation rate at the surface. The remaining parameter space for the simulation consists of the SiH_4 pressure, surface temperature, adsorbate–adsorbate binding energy, adsorbate–substrate binding energy, and ratio of the migration energy to the desorption energy.

In order to limit the parameter space and gain insight into the deposition of silicon, a single adsorbate–adsorbate binding energy $E_{a\text{-}a} = 2.0$ eV is chosen. This value produces an adsorbate atom desorption energy from a surface layer of adsorbate atoms of 3.2 eV. This desorption energy is consistent with that obtained by equating the rate of desorption [given by the reciprocal of Eq. (8)] to the equilibrium rate of flux at the surface over the temperature range $1000 < T < 1600$ K. This equilibrium rate is given by $n\nu/4$, where $n = P_{\text{vap}}/kT$ and where P_{vap} is the vapor pressure of silicon.[55] This bond energy is representative of a strong adsorbate–adsorbate attraction.

Surveying the experimental values of adatom migration and desorption energies of various material systems, it was observed that the ratio of migration energy E_m to desorption energy E_d is generally expressed by the inequality $\frac{1}{4}E_d < E_m < \frac{2}{3}E_d$ for most adsorbate–substrate combinations,[53] excluding cases of the desorption and migration of inert gas atoms. Since the desorption and migration energies of silicon on surfaces of c-Si, SiO_2, and $Si_x N_y$ are not precisely known, a constant value of $E_m = 0.51\ E_d$ was chosen for the purpose of this study, so that $f = 0.5$ here.

Claassen and Bloem[8] estimate an upper limit for the migration energy E_m of Si on surfaces of SiO_2 of 0.4 eV, and their experimental results suggest that the migration energy of Si on surfaces of $Si_x N_y$ is slightly larger. The adsorbate–substrate binding energy was adjusted over a range of values to provide an adatom substrate migration energy E_m between 0.45 and 0.70 eV. At the higher migration energies, it was found that the sticking probability of an adatom produced at the surface approached unity and increasing the migration energy to larger values did not change the nucleation characteristics.

To determine a suitable size for the simulation grid, the value of Λ, the average distance an adatom migrates before desorbing, given by Eq. (10), must be estimated. This value scales as the ratio of E_m/kT. For $E_m = 0.7$ eV and for temperatures $T > 1000$ K, $\Lambda \leqslant 55d$, where d is the average migration distance on the surface. For silicon $d = 2.7$ Å, and this value is used in the simulation for surfaces of SiO_2 and $Si_x N_y$ as well. Thus, $\Lambda \leqslant 150$ Å. At lower migration energies the value of Λ decreases rapidly. As a practical tradeoff between the decrease in available computer time with an increase in memory requirements, the simulation grid surface area was set to $55 \times 55 \times 10$.

The laser-induced temperature change over a grid area this size is < 20 K for the highest laser power example depicted in Fig. 1, so a uniform surface temperature is used within each grid. The simulation was run over a pressure range from 0.2 to 10 Torr, and a temperature range of 600–1600 K. Even though Λ becomes greater than the size of the grid at temperatures below 1000 K at migration energies of $E_m \sim 0.7$ eV, the simulation showed that in this regime adatom clustering occurred almost instantaneously and the number of adatoms crossing the boundary is not significantly greater than when Λ is less than the grid size, thus validating this choice of grid size.

In order to relate the simulation results to the micron-dimensional reaction area encountered in LLCVD, a laser power and spot size at the surface are specified and the resulting laser-induced temperature distribution is calculated. The results of a particular simulation at a given temperature are associated with a specific area of the laser-heated region at that temperature. In this way, the nucleation simulation which covers an area of $2.25 \times 10^{-4}\ \mu\text{m}^2$ (150×150 Å, 55×55 atomic sites) samples the dynamics of a small but representative region of the laser-irradiated surface. The relation of the simulation results to LLCVD is discussed in Sec. V.

B. General features of nucleation kinetics

Figure 4 shows isometric plots of the surface topology as a function of time for deposition onto a strongly binding substrate and a moderately strong binding substrate. The conditions in Figs. 4(a) and 4(b) simulate a SiH_4 pressure of 10 Torr, a substrate temperature of 1400 K, and a migration energy of 0.60 and 0.50 eV, respectively. The migration and desorption of two-atom clusters in addition to those of single adatoms were allowed in these simulations. For the $E_m = 0.60$ eV case [Fig. 4(a)], silicon growth occurs almost instantaneously. The incubation time, which is defined here as the time between the start of the deposition process and the time when a few dimers have nucleated on the surface, is $\leqslant 1\ \mu$s. Clustering of atoms initiates immediately and 27% of the total number of atoms produced at the surface have stuck by the time 5% surface coverage is obtained, 37% have stuck by the time 10% surface coverage is obtained, while 50% of the atoms have stuck by the time 20% surface coverage is obtained. Thus, between 5% and 10% surface coverage, the differential sticking coefficient was 59% while between 10% and 20% surface coverage it rose to 77%. The surface coverage is defined here as the number of deposited atoms divided by the number of surface sites. This type of initial morphology, with a higher cluster density [Fig. 4(a)], is expected when depositing silicon onto a strongly binding substrate, such as a silicon substrate.

In contrast to the above case, when $E_m = 0.50$ eV [Fig. 4(b)], nucleation is no longer instantaneous and begins to play a significant role in thin film growth. Here, a longer (although still insignificant with respect to typical dwell times) incubation period of $\sim 3\ \mu$s is seen to occur and the

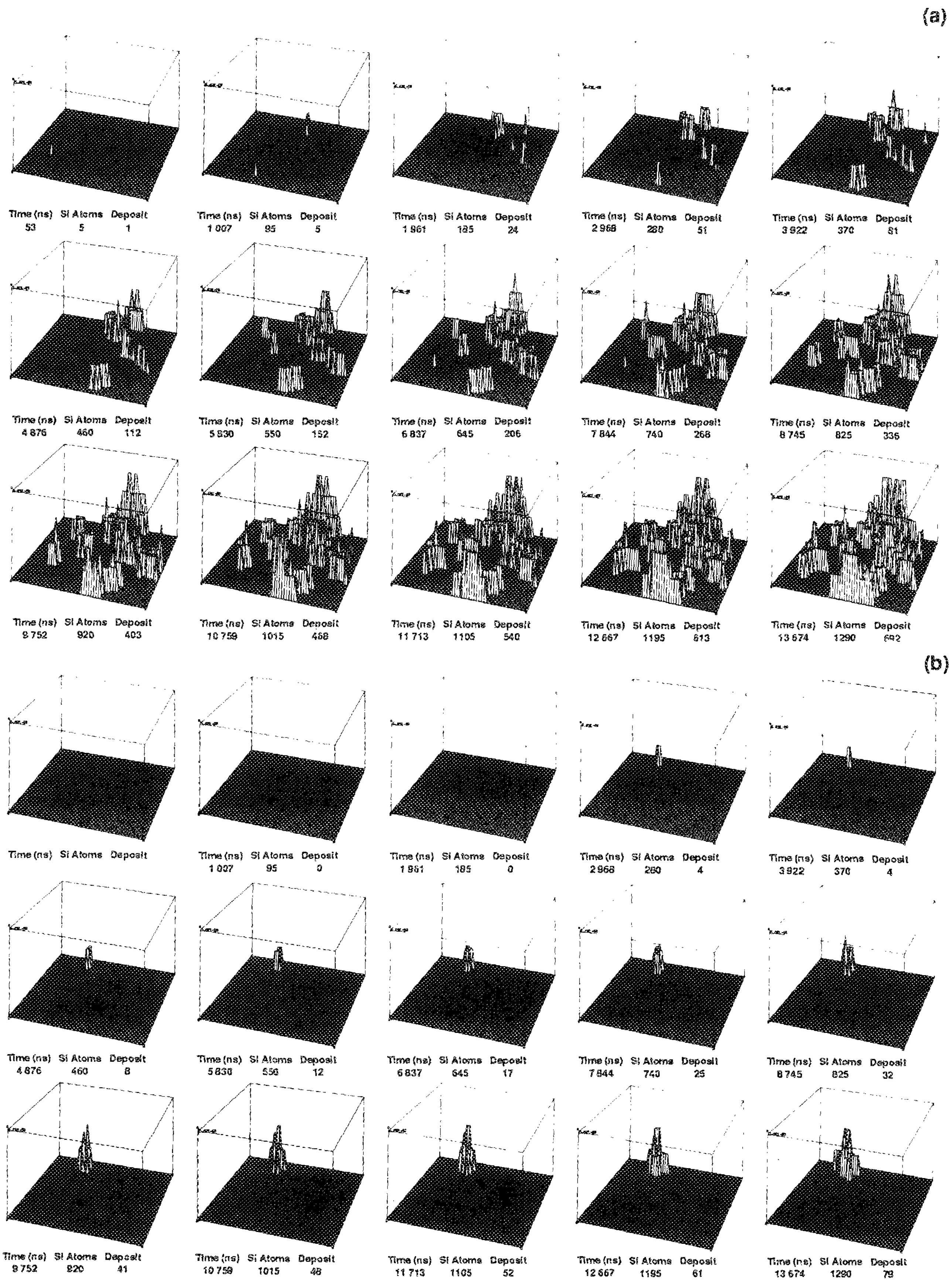

FIG. 4. Isometric plots of the surface topology as a function of time for a silane pressure of 10 Torr, a substrate temperature of 1400 K, and migration energy (a) $E_m = 0.60$ eV and (b) $E_m = 0.50$ eV. Both single adatom and two-atom cluster dynamics are included in the simulation. Notice the distinction between clusters with 1, 2, and 3 atoms high.

density of critical nuclei is greatly reduced. In this case, the growth rate does not begin to approach that predicted by Eq. (7) until long after the start of deposition. At 5% surface coverage, only 9% of the atoms produced at the surface remain and contribute to the growing film compared to 27% when $E_m = 0.60$ eV. The film growth is characterized predominantly by continued growth of a few nucleated islands of silicon. Thus, larger grain sizes would develop and the thin film thickness at which a contiguous film would be produced is increased for $E_m = 0.50$ eV compared to the $E_m = 0.60$ eV case. Since the binding energies of silicon to surfaces of SiO_2 and Si_xN_y are reported to be lower than the values used in the above simulation, the incubation period prior to nucleation is expected to be even longer and the critical cluster density to be further reduced than for the results shown above. These two figures, 4(a) and 4(b), are meant to show the qualitative difference in the thin film nucleation morphology at the crossover between "strong" and "moderately strong" adsorbate-substrate binding energies.

Even though the formulation of the model allowed interstitial vacancies to form during thin film growth, for the simulation conditions reported here vacancies did not influence the initial thin film composition. The data in Figs. 5–10 included only the dynamics of single adatom migrations and desorptions; the effects of two-atom cluster migrations and desorptions were not included.

C. Initial growth rate versus time

The amount of silicon deposited as a function of time for a silane pressure of 10 Torr is shown in Fig. 5, for adsorbate–substrate migration energies of (a) 0.60, (b) 0.50, and (c) 0.45 eV and temperatures ranging between 600 and 1600 K. For $E_m \geqslant 0.60$ eV, deposition occurs almost instantly for all temperatures and the initial stage of film growth is characterized by a large number of small (<10 atom) clusters. Two-atom cluster dynamics are not included in these simulations.

For $E_m = 0.50$ eV [Fig. 5(b)], deposition is qualitatively the same as for $E_m = 0.60$ eV from $T = 600$–1400 K. However, an incubation period of ~ 30 μs is observed at a temperature of 1600 K which is not observed for the $E_m = 0.60$ eV case. Once this incubation period is over, growth at this temperature proceeds quickly due to the high rate of molecular dissociation. At 1600 K, adatom desorption dominates over adatom migration, so material initially nucleates faster at lower temperatures. This result is in conflict with the intuitive perception that most of the material will be deposited at the higher temperatures due to the monotonically increasing rate of molecular dissocation with increasing temperature. The two growth curves at 1600 K, representing two different Monte Carlo simulations, give some indication of the statistical uncertainty inherent in the nucleation process. At $T = 1600$ K, the density of nuclei is reduced with most of the material deposited around one or two nuclei [as in Fig. 4(b)].

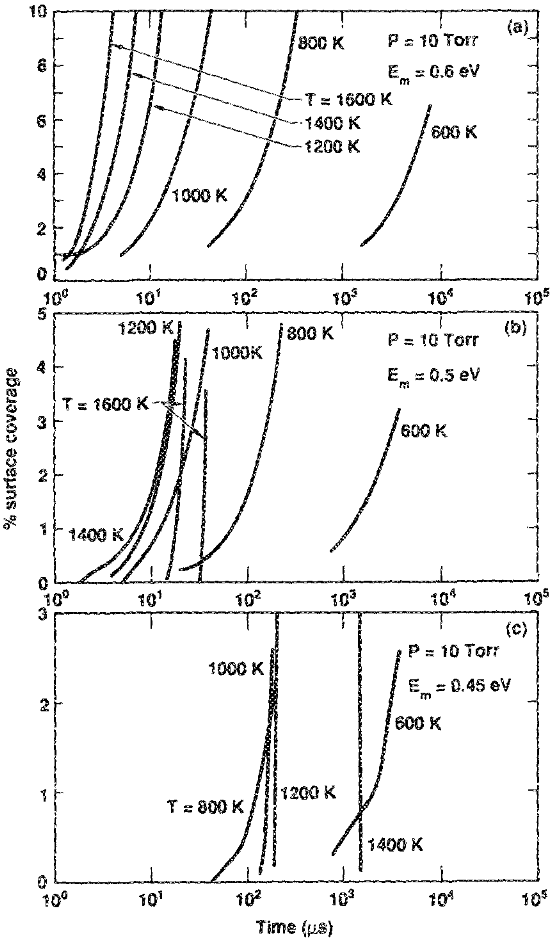

FIG. 5. Percent of surface coverage in monolayers as a function of time for a silane pressure of 10 Torr and migration energy (a) $E_m = 0.60$ eV, (b) $E_m = 0.50$ eV, and (c) $E_m = 0.45$ eV at the temperatures indicated.

For $E_m = 0.45$ eV [Fig. 5(c)], the limitations of nucleation become much more important even at lower temperatures than for the $E_m = 0.50$ eV case. For T between 600 and 800 K, nucleation proceeds in a manner similar to that in Figs. 5(a) and 5(b). However, at temperatures above ~ 1000 K the incubation period becomes more pronounced resulting in less initially deposited material for $T > 1000$ K, than at lower temperatures. At a temperature of 1600 K, no nuclei formed on the surface during the simulation even after 5 ms of deposition. Because the total number of events between incident reactant molecules Ψ increases with these lower migration energies, the amount of computer time needed to simulate the same surface coverage increases and therefore only a lower total surface coverage could be examined in these cases.

Thus two regimes of initial growth can be distinguished from the data of Figs. 4 and 5. As the substrate temperature T is increased up to a critical temperature T_c, greater numbers of deposit atoms are produced at the surface per second which results in an increased rate of growth of deposited material. At temperatures $T > T_c$, the rate of deposit atom production continues to increase with temperature, but adatom migration which leads to eventual clustering is dominated by adatom desorption; this results in a reduction of the amount of material deposited onto the substrate. However, once nuclei form on the high temperature substrates (perhaps after a long incubation time) growth proceeds

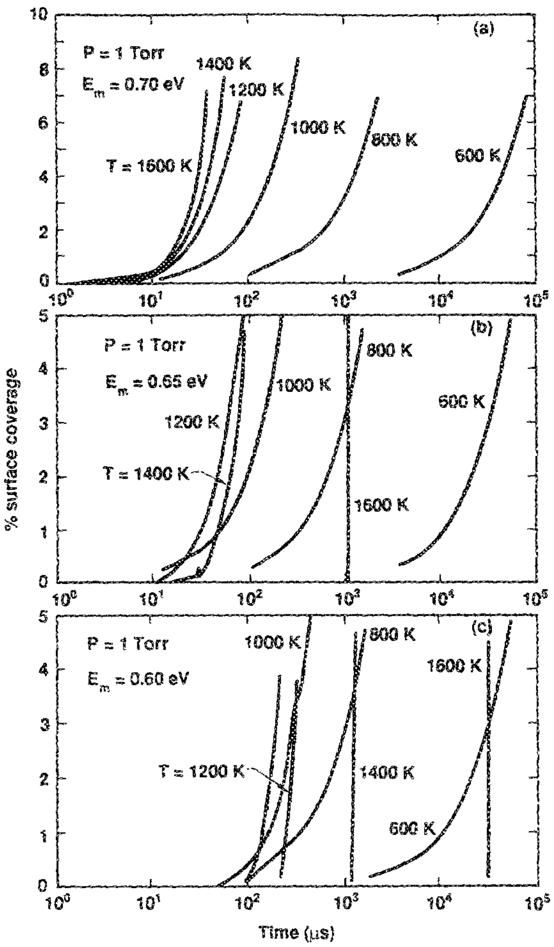

FIG. 6. Percent of surface coverage in monolayers as a function of time for a silane pressure of 1 Torr and migration energy (a) $E_m = 0.70$ eV, (b) $E_m = 0.65$ eV, and (c) $E_m = 0.60$ eV at the temperatures indicated. In (c) there are two nearly parallel plots for $T = 1200$ K: the plot first crossed by the arrow and the plot pointed to by the arrow.

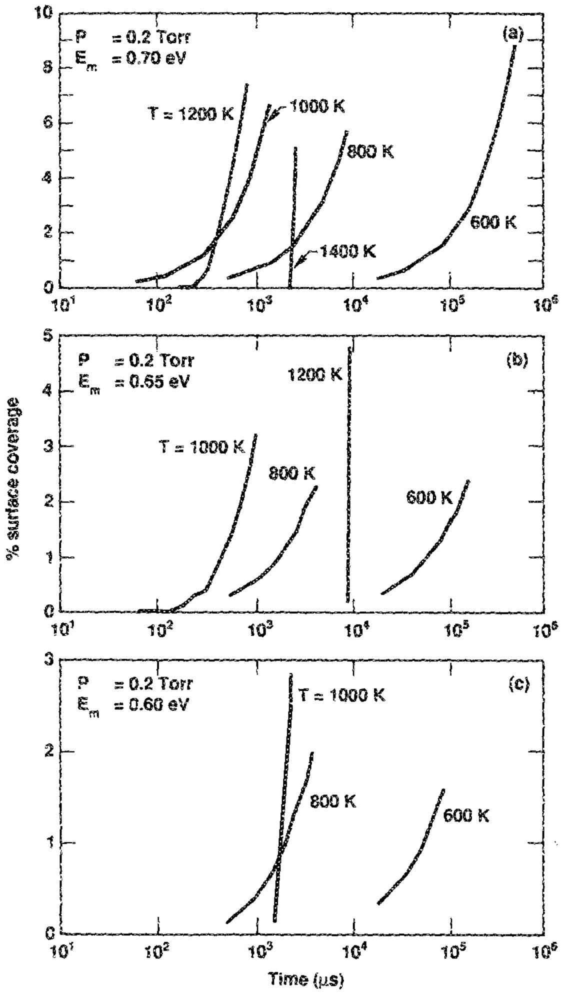

FIG. 7. Percent of surface coverage in monolayers as a function of time for a silane pressure of 0.2 Torr and migration energy (a) $E_m = 0.70$ eV, (b) $E_m = 0.65$ eV, and (c) $E_m = 0.60$ eV at the temperatures indicated.

quickly due to the fast rate of adatom formation at high temperatures.

The amount of deposited material versus time at silane pressures of 1 and 0.2 Torr is shown in Figs. 6 and 7. At a SiH_4 pressure of 1 Torr, the critical temperature $T_c \sim 1600$ K at $E_m = 0.70$ eV, $T_c \sim 1400$ K at $E_m = 0.65$ eV, and $T_c \sim 1200$ K at $E_m = 0.60$ eV. When the SiH_4 pressure is reduced to 0.2 Torr, the critical temperature reduces further to $T_c \sim 1400$ K at $E_m = 0.70$ eV, $T_c \sim 1200$ K at $E_m = 0.65$ eV, and $T_c \sim 1000$ K at $E_m = 0.60$ eV. At a pressure of 1 Torr and $E_m = 0.60$ eV, the results of two simulation runs are again shown to indicate the statistical uncertainty in the growth process. For $P = 0.2$ Torr, no nuclei are observed even after 0.5 s when $E_m \leqslant 0.65$ eV and $T > 1200$ K. As the pressure is decreased, the critical temperature T_c is found to shift towards lower temperatures for the same adsorbate–substrate migration energy.

The region of parameter space where an incubation period prior to nucleation will strongly influence the initial thin film morphology is demarked in Fig. 8 as a function of the adsorbate-migration energy, temperature, and SiH_4 gas pressure. For deposition conditions which fall below the lines in Fig. 8, deposition occurs without delay, while for

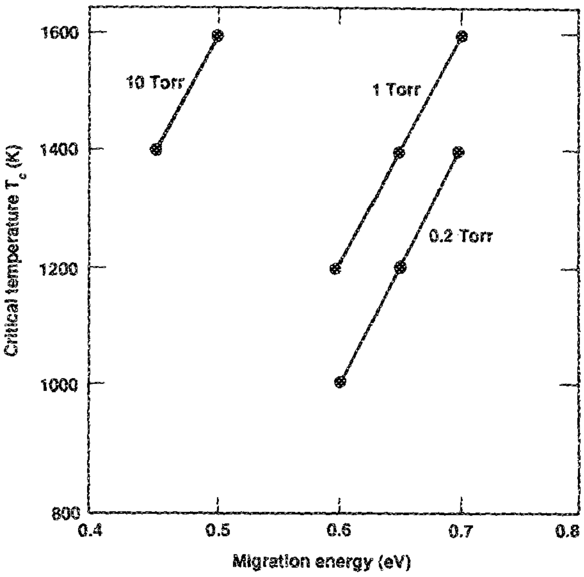

FIG. 8. Critical temperature T_c as a function of migration energy and silane pressure. At deposition temperatures below the critical temperature, nucleation occurs immediately with no apparent incubation period; for temperatures above T_c, a long incubation period exists before nucleation begins. The simulations are run at temperatures from 600 to 1600 K in 200 K increments. For $E_m = 0.6$ eV, $T_c > 1600$ K at 10 Torr.

conditions above the lines, an incubation period before the onset of deposition is observed. For $P = 10$ Torr and $E_m = 0.60$ eV, $T_c > 1600$ K, the highest temperature simulated. A rough analytic estimate of this critical temperature T_c can be obtained by equating the rate of adatom desorption $1/\tau_d$ [the reciprocal of Eq. (8)] with the rate of adatom formation R_{Si} [Eq. (7)] within a characteristic migration circle of area $\pi(\Lambda/d)^2$, where Λ is the average distance an adatom migrates before desorption [Eq. (10)]. Assuming $E_m = 0.51E_d$,

$$T_c \sim 3.34\times 10^4\left(\frac{E_m - 0.255}{12.3 - \log P_{\mathrm{SiH}_4}}\right), \qquad (23)$$

where T_c is in Kelvin, E_m is in eV, and P_{SiH_4} is in Torr. For example, for a pressure of 10 Torr, the estimated critical temperatures are $T_c = 1150, 810, 650$ K for migration energies $E_m = 0.60$, 0.50, and 0.45 eV, respectively, which are somewhat lower than T_c from the simulations. The importance of T_c in determining the initial morphology of deposited material during LLCVD is discussed in Sec. V.

To examine the pressure dependence of the nucleation rate clearly, the amount of deposited material normalized by the silane pressure is plotted in Fig. 9 as a function of time for various pressures. The migration energy is $E_m = 0.60$ eV, and the substrate temperatures are (a) $T = 800$ K, (b) $T = 1200$ K, and (c) $T = 1600$ K. The amount of material that would be deposited as a function of time assuming a unity sticking coefficient given by Eq. (7) is also plotted in the figures. For a temperature of 800 K, the change in pressure between 0.2 and 10 Torr results in an increase in deposition rate which is approximately linear in pressure, and therefore only relatively small differences exist in these normalized plots, and the overall sticking coefficient of a silicon adatom is nearly unity. As the temperature increases to 1200 K, a nonlinear dependence of the initial deposition rate versus pressure becomes apparent. This is indicated by both an incubation delay before nucleation and also a decrease in the slope of the growth rate with lowered pressure. At a temperature of 1600 K, the deposition rate is highly nonlinear in pressure. The two curves for the 1-Torr data in Fig. 9(b) refer to the results of two different simulation runs whose data are shown in Fig. 6(c). For the 1-Torr data in Fig. 9(c), a delay of 33 ms was subtracted from the time axis in order to display the data on the same graph; substantial deposition begins after 35 ms.

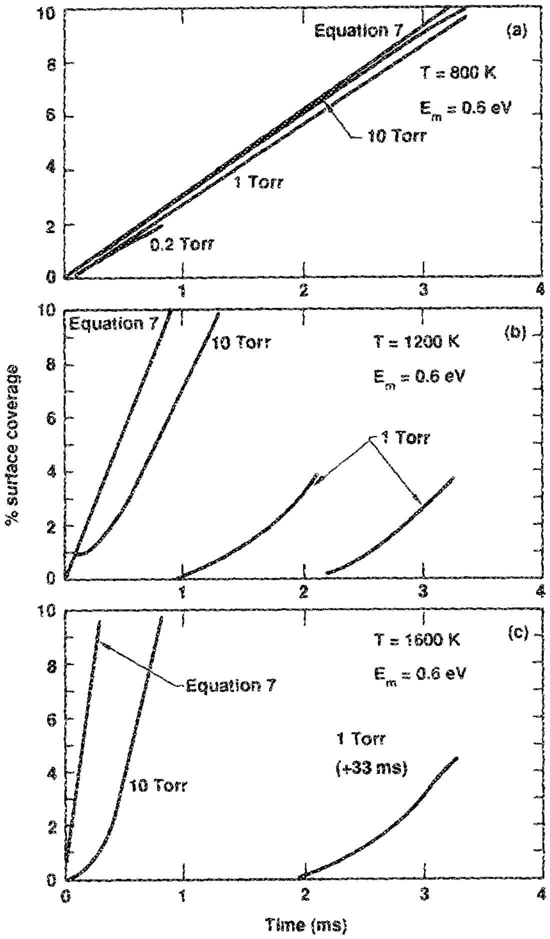

FIG. 9. Percent of surface coverage in monolayers as a function of time with the rate of incident silane molecules normalized to that occurring at a pressure of 1 Torr, and with $E_m = 0.6$ eV and a substrate temperature of (a) 800 K, (b) 1200 K, (c) 1600 K at the pressures indicated.

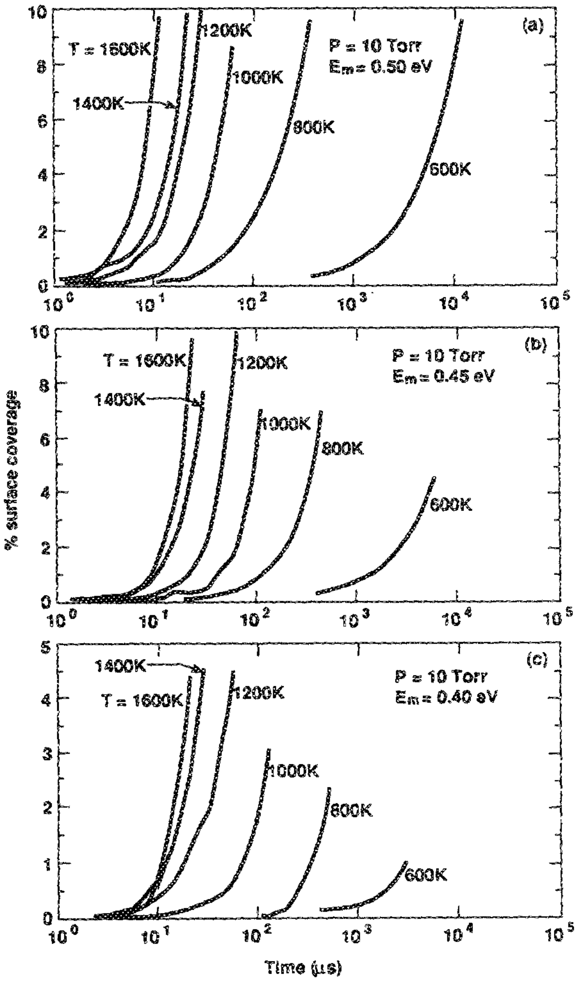

FIG. 10. Percent of surface coverage in monolayers as a function of time when a nucleation site is located at the center of the simulation grid for a silane pressure of 10 Torr, migration energy of (a) $E_m = 0.50$ eV, (b) $E_m = 0.45$ eV, and (c) $E_m = 0.40$ eV, and temperatures indicated.

D. Role of impurities and defects

In order to simulate the effects of impurities and defects, a single "nucleation site" corresponding to an infinitely deep binding site is located at the center of the simulation grid. This corresponds to a fraction of 3.3×10^{-4} permanent nucleation sites on the substrate surface. Since experimental surface analysis techniques have a resolution on the order of one part per thousand, this density of nucleation sites could exist on an experimentally "clean" surface. Figure 10 shows the percent of surface coverage as a function of time for a silane pressure of 10 Torr, and migration energies $E_m = 0.50, 0.45$, and 0.40 eV. The addition of the nucleation sites effectively eliminates the incubation period, except possibly for extremely low adsorbate–substrate migration energies and at high temperatures. Thus, the critical temperature becomes greater than the melting temperature of silicon $T_c > 1690$ K.

E. Role of dimer migrations

The additional dynamics of two-atom cluster migrations and desorptions were simulated for a SiH_4 pressure of 10 Torr, and migration energies $E_m = 0.45$, 0.50, and 0.60 eV assuming no defects. The amount of surface coverage as a function of time is shown in Fig. 4 and the influence of dimer dynamics on the initial rate of thin film growth is obtained by comparing these results with those of Fig. 5 which are for the same deposition conditions but include only single adatom dynamics. In general, at high migration energies $E_m > 0.50$ eV or at low temperatures $T < 1200$ K the addition of dimer dynamics does not affect the nucleation rate. This can be explained by the fact that in this model, the activation energy for dimer migration and desorption is much greater than that for single adatoms, and hence the dimer dynamics do not become activated at low temperatures. At low migration energies and high temperatures, dimer migrations do take place and serve to decrease the incubation time.

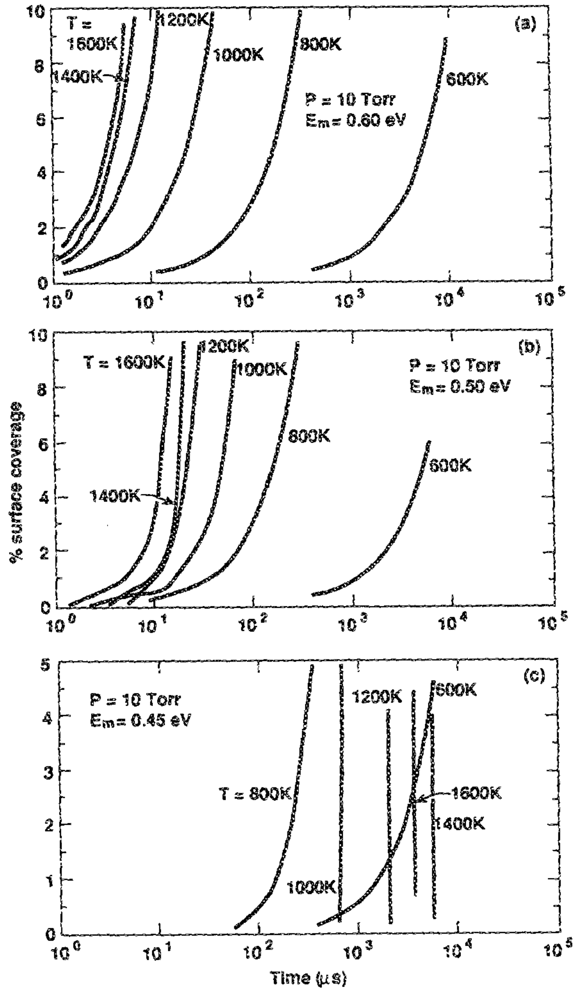

FIG. 11. Percent of surface coverage in monolayers as a function of time when dimer migrations are included in the simulation for a silane pressure of 10 Torr and migration energy of (a) $E_m = 0.60$ eV, (b) $E_m = 0.50$ eV, and (c) $E_m = 0.45$ eV.

For example, at $E_m = 0.50$ eV [Fig. 11(b)] and $T = 1600$ K, approximately 450 dimer migrations took place and zero dimer desorptions occurred during the simulation. This is a small value compared to the approximately 135 000 single adatom migrations and 4500 single adatom desorptions which also took place during the same simulation run. The number of null events was greater than 71 000 000. The increasing number of dimer migrations with increasing temperature causes the incubation period to decrease. The incubation period at $T = 1600$ K is only $\sim 1.5\,\mu$s which is less than the incubation period of $\sim 15\,\mu$s which is observed when dimer migrations are not included [Fig. 5(b)]. The critical temperature increases from a value of $T_c \sim 1600$ K without dimers to a value >1600 K with dimers.

For $E_m = 0.45$ eV [Fig. 11(c)] the incubation period increases when increasing the temperature from 1000 to 1400 K as it does when dimer migrations are not included. But, the incubation period decreases slightly when the temperature is raised to 1600 K because of the increased mobility and increased clustering by dimer aggregates. The decrease in incubation time with increasing temperature after an initial increase in the incubation time with increasing temperature is observed only when dimer migrations are included in the simulation.

V. NUCLEATION EFFECTS IN LLCVD

A. Static laser irradiation

Insight into the role of nucleation during LLCVD for static laser irradiation can be obtained now by matching the results of the initial growth rate and cluster density from the Monte Carlo simulation (Secs. IV C–IV E) with the laser-induced surface temperature profile (Sec. II B). In essence, the Monte Carlo simulation is used to sample a small area of the laser-heated region of the surface while the thermal calculation provides the connection between a specific temperature and its corresponding location on the substrate surface. Since the grid length is less than the migration distance, and the temperature gradient across the grid size is small, this approach is valid as stated earlier.

Figure 12 is an illustration of the predicted initial thin film morphology based on the simulation results of Sec. IV. For laser-induced peak temperatures $T_p > T_c$, the most probable location for the initiation of thin film growth is radially displaced from the center of the locally laser-heated

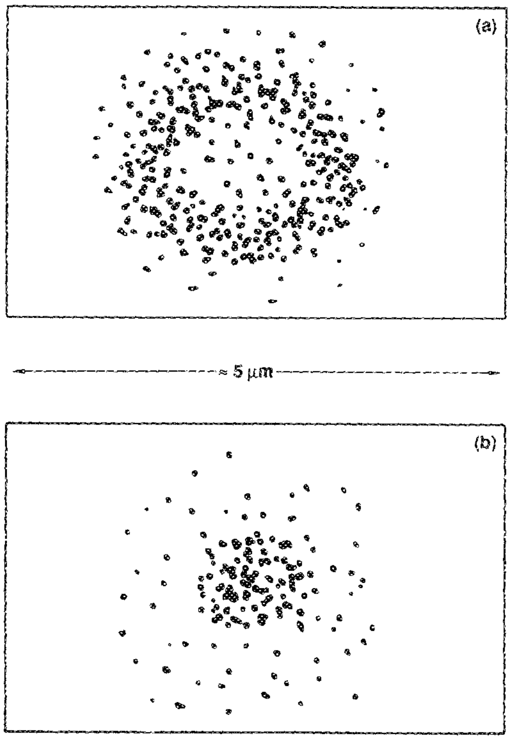

FIG. 12. Schematic representation of the initial growth morphology in LLCVD for (a) the peak temperature greater than the critical temperature $T_p > T_c$, (b) the peak temperature less than the critical temperature $T_p < T_c$.

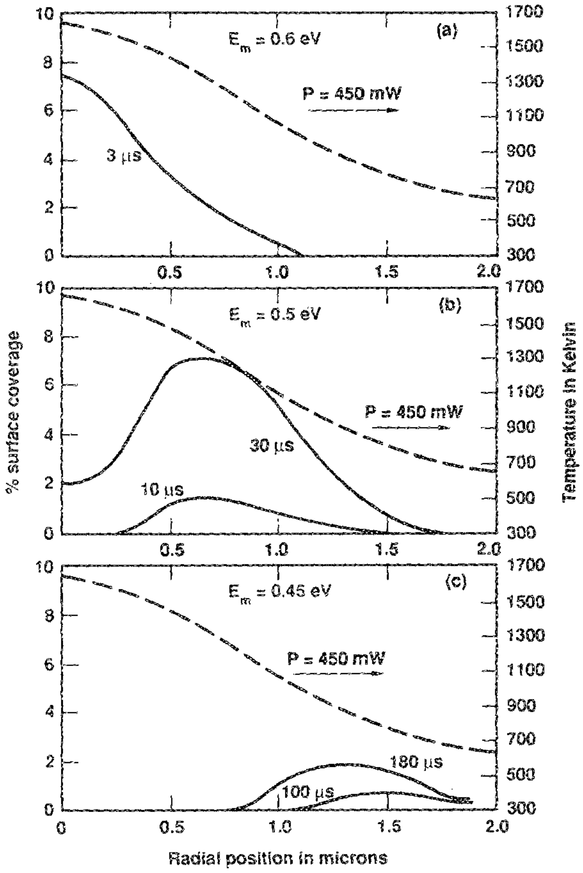

FIG. 13. Initial thin film morphology (—) as a function of radial position for the temperature profile (- - -) and time indicated, a silane pressure of 10 Torr and migration energy of (a) $E_m = 0.60$ eV, (b) $E_m = 0.50$ eV, and (c) $E_m = 0.45$ eV.

region of the surface as shown schematically in Fig. 12(a); while for $T_p < T_c$, thin film nucleation is found to begin at the center of the locally laser-heated region surface Fig. 12(b). If dimer migrations contribute to nucleation, the initial morphology may consist of deposited material in the center of the laser-heated region in addition to an annulus region when $T_p > T_c$.

Analyzing deposition for the computed laser-induced temperature profile of Fig. 1 for an incident laser power of 450 mW, and using the predicted surface coverage as a function of time for 10 Torr of SiH_4 at adsorbate-substrate migration energies $E_m = 0.60$, 0.50, and 0.45 eV from Fig. 5, the radial profile of the initial thin film morphology at various times can be obtained and is shown in Fig. 13. The temperature profile from Fig. 1 is also replotted in this figure. For $E_m = 0.60$ eV [Fig. 13(a)], most of the deposited material occurs at the center of the laser-heated region and the initial deposit of material is more highly spatially confined than the laser induced temperature profile as is expected for $T_p = 1650$ K and $T_c > T_{\text{melt}}$.

For $E_m = 0.50$ eV and $E_m = 0.45$ eV [Figs. 13(b) and 13(c)] the initial deposit of material is displaced from the center of the laser-heated region and takes the form of an annulus because $T_p = 1650$ K is $> T_c \sim 1400 K$ ($E_m = 0.50$ eV) and $T_c \sim 1000$ K ($E_m = 0.45$ eV). Thin film growth in the unnucleated central region of the surface can result either from the inward growth of the annulus (i.e., by deposition onto the already nucleated inner ring of the annulus) or by nucleation in the central region at a later time. For $E_m = 0.50$ eV [Fig. 13(b)] nucleation initially begins at a radial distance of $\sim 0.7\,\mu$m. After $\sim 30\,\mu$s, nucleation is seen to begin at the center of the laser irradiation region causing the central region to fill in quickly. For $E_m = 0.45$ eV [Fig. 13(c)] the annulus region is displaced even further from the center and then grows inward, but even after 5 ms, the central region does not begin to nucleate. Note that as E_m decreases, the radius of the initially formed annulus deposit and the incubation period both increase. Also, in these cases, growth in the center appears to begin by nucleation in the center for $E_m = 0.50$ eV and by continued growth on the inside region of the annulus for $E_m = 0.45$ eV.

The inclusion of nucleation sites tends to increase T_c. LLCVD growth on clean surfaces may begin with an annulus morphology, but surface impurities may force nucleation in the center even for very weak adsorbate-surface binding energies.

Baranauskas *et al.*[19] measured the nucleation and initial growth of silicon deposited from $SiCl_4$ onto surfaces of quartz during LLCVD. They identified three regimes of initial thin film morphology. At low substrate temperatures, $T \sim 1360$ K, nucleation was observed immediately but only in the center of the irradiated region of the surface, and the vertical growth rate of Si islands was much higher than the lateral rate. At intermediate peak temperatures, $T \sim 1650$ K, nuclei grew into islands which later coalesced to form a uniform thin film out to a temperature of $T \sim 1200$ K where an etching reaction of the $SiCl_4$ predominated. Thin films grown at high peak temperatures, $T = 1750$ K, nucleated in the cooler region of the irradiated substrate and coalesced into a continuous annulus. The center of the annulus eventually filled in with material after a sufficiently long time.

In these cited experiments, a CO_2 laser at a wavelength 10.6 μm was focused to a diameter of ~ 3 mm to induce a heated region on the quartz substrate surface. A mixture of 12% $SiCl_4$ in H_2 was flowed across the substrate surface. The maximum observed growth rate was only $\sim 10\,\mu$m/min and since the resulting annulus deposit of material was symmetric with respect to the incident laser irradiation for peak temperatures of 1750 K, it is unlikely that gas phase diffusion was responsible for limiting the deposition rate in the center. The observation of the difference between the low and intermediate temperature regimes, and the high temperature regime, is in accord with the simulation results reported here.

In several studies of static LLCVD, volcanolike disk deposits with depressed centers or donutlike structures have been observed. In the deposition of nickel[56] and gold,[24] these morphologies have been observed in the post-nucleation growth phase with thick (~ 0.1 several μm) deposits. These morphologies are probably not due to the nucleation-induced effect which leads to the annulus geometry predicted here, but due either to starvation of reactant molecules at the center, enhanced photon-induced surface reactivity, or viscosity effects for molten deposits.

B. Scanning laser irradiation

A substrate surface is patterned during LLCVD by scanning the focused laser with respect to the surface. The nucleation stage of thin film growth is much more complex in this case compared to static laser heating because of the time-dependent temperature profile established on the surface as the leading and trailing edges of the laser spot traverse the point of examination on the surface. A schematic representation showing possible effects of nucleation during scanning LLCVD is shown in Fig. 14. There are three fundamentally different steady-state growth conditions possible. In the first case [Fig. 14(a)] only the nucleation stage of thin film growth is obtained during scanning. This regime is not of any practical interest, but can be used as a benchmark to obtain an estimate of the maximum scanning speed at which deposition can take place. In the second case, thin film growth occurs by nucleation onto the laser irradiated region as in part (a), but also by the continued growth onto the previously written feature [Fig. 14(b)]. A final case of thin film growth during scanning-laser irradiation results when the thin film material is primarily deposited onto the already grown feature and little growth occurs due to nucleation in the laser irradiated region [Fig. 14(c)]. Growth under this last condition may be accompanied by very low adhesion of the feature to the surface since very little of the film is actually grown from the surface.

Since the simulations presented here deal with the nucleation phase of deposition only and do not involve the continued growth or steady-state growth stage, the results of Sec. IV can be used only to examine the case shown in Fig. 14(a) and to predict the maximum scan speed at which nucleation can occur. As stated in Sec. II B, a steady-state temperature is reached during laser scanning as long as the dwell time $\tau_{\text{dwell}} = S/v > S^2/D$, where S is the laser spot diameter, v is the scan velocity, and D is the thermal diffusivity. For micron-dimensional spot sizes, and a silicon substrate, this inequality is valid for scanning speeds $v < 1$ m/s. Thus, for scan velocities of a few mm/s, a few micron diameter beam will have a dwell time of ~ 1 ms, which is sufficiently long for local steady state to be maintained. Therefore, the time-dependent temperature at position Y perpendicular to the scanning direction can be obtained from

$$T[Y(t)] = T[(v^2t^2 + Y^2)^{1/2}].$$

Using the results of the laser-induced steady-state temperature profile shown in Fig. 1 for a laser power of 450 mW, the time-dependent temperature profile for a scanning laser

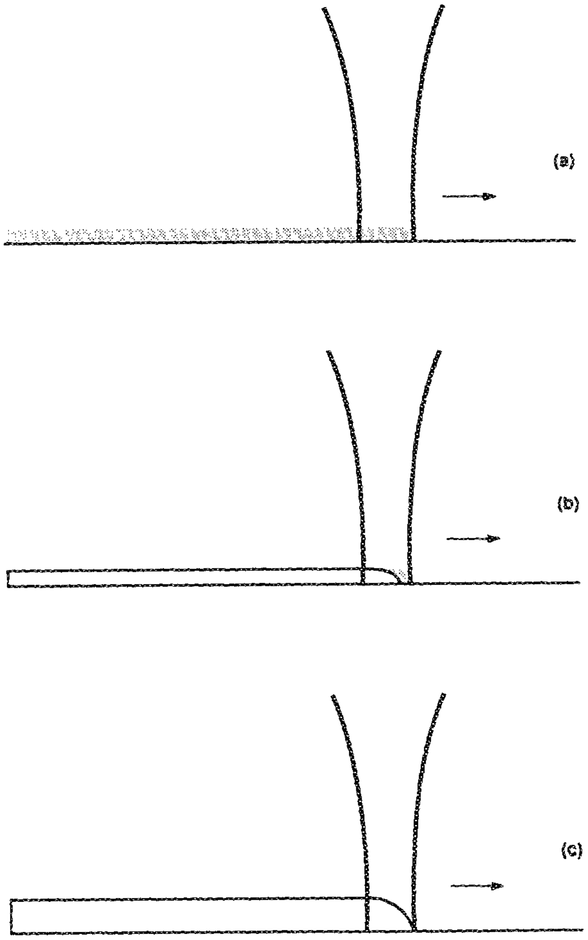

FIG. 14. Schematic representation of three modes of nucleation and thin film growth during scanning LLCVD: (a) the laser is scanned at the maximum velocity v_m for nucleation to just occur; (b) the scan velocity is decreased and thin film growth takes place both by continued growth onto an already written feature and by growth of nuclei in the advancing edge of the laser; and (c) material growth takes place exclusively on an already written thin film segment, resulting in the possible low adhesion of the film to the substrate.

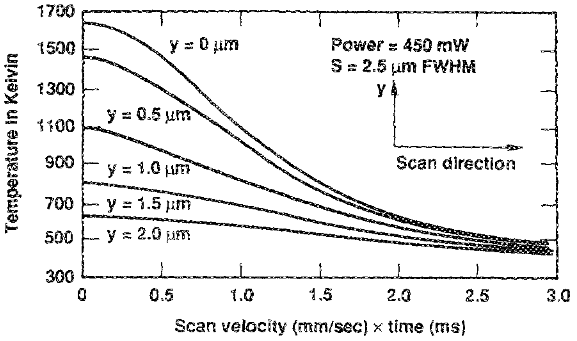

FIG. 15. Time-dependent temperature response produced by scanning a Gaussian laser with 450 mW of power at a wavelength of 514.5 nm and a 2.5 μm FWHM diameter across a 50-nm thick SiO_2 film on a silicon substrate. At time $t = 0$ the peak of the laser is at the point of reference.

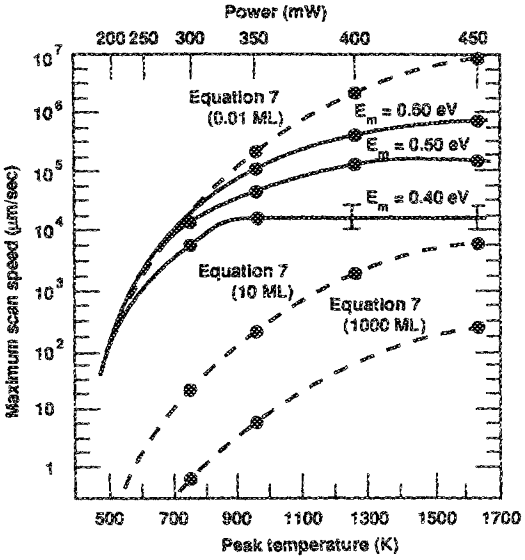

FIG. 16. Maximum scan velocity v_m to provide 0.01 monolayers (ML) of silicon as a function of peak surface temperature T_p for different adsorbate–substrate binding energies at a SiH_4 pressure of 10 Torr (—). Also plotted are the scan velocities to produce 0.01, 10, and 1000 ML of material assuming instant nucleation as a function of peak temperature from Eq. (7) (- - -). These plots refer to the center of the scan, $Y = 0.0\,\mu$m.

across the surface at the center of the laser irradiation, and at distances $Y = 0.0$, 0.5, 1.0, 1.5, and 2.0 μm perpendicular to the scan direction are obtained, and shown in Fig. 15. The $Y = 0.0\,\mu$m case is the same as the 450-mW curve in Fig. 1 but the abscissa differs by a factor of the scan velocity v. At $t = 0$, the laser is centered with respect to the particular location on the surface being examined.

Using the incubation times from the simulation results of Sec. IV and the dwell times from the time-dependent temperature profile, the scan velocity which will produce just the nucleation phase of thin film growth as depicted in Fig. 14(a), can be predicted for various peak temperatures and adsorbate–substrate binding energies. This scan velocity v_m then represents an upper limit to the speed at which 0.01 monolayers of surface coverage can be obtained during LLCVD. This is an important quantity in laser prenucleation patterning experiments, such as those reported by Tsao and Ehrlich.[17,18] At corresponding slower scan speeds, substantially thicker deposits can be formed.

Consider the amount of material deposited at only the center of the scanning laser. Simulation results show that once ~1% of a monolayer coverage is obtained, thin film growth proceeds quite rapidly at a rate given essentially by Eq. (7). Thus, a 1% coverage will be used here as a criterion for nucleation during scanning laser deposition. Consider the data for 10 Torr of SiH_4 given in Fig. 5, the temperature profiles of Fig. 1, and the time dependence shown in Fig. 15. For $E_m = 0.60$ eV, $T_p < T_c$ for all laser powers considered. Thus, the fastest nucleation will occur during the highest temperatures encountered during the scan. The maximum scan speed (v_m) leading to nucleation is estimated by equating the dwell time near the peak temperature $[\sim S/v_m(T_p)]$ to the incubation time at that temperature.

For $E_m = 0.50$ and 0.45 eV, more material is deposited as the laser power increases only when the peak temperatures $T_p < T_c$. For these cases an estimate of v_m is obtained as in the $E_m = 0.60$ eV case. When $T_p > T_c$, the shortest incubation time no longer occurs at the peak temperature in the scan, but at some lower temperature. Thus, most of the nuclei will form during the leading edge of the temperature profile, before the peak temperature is reached. A careful estimate of the maximum scan velocity which would still result in 1% surface coverage in this regime is complicated by the fact that nucleation occurs during the leading edge of the temperature profile. Continued growth will then proceed rapidly at peak temperatures $T_p < T_c$ resulting in more than 1% surface coverage. Still a good estimate of v_m for $T_p > T_c$ can be obtained by requiring that nucleation occur during the leading edge of the temperature profile and finding the maximum velocity for which the dwell time in a given temperature range during the leading edge equals the incubation time for that temperature range.

Figure 16 shows the maximum scan velocity v_m which could be used to obtain 1% surface coverage as a function of the peak temperature (laser power) and adsorbate–substrate binding energy, for a silane pressure of 10 Torr. Also plotted in Fig. 16 is the scan velocity which could be used to deposit 1% of a monolayer, as well as 10 monolayers (27 nm) and 1000 monolayers (0.27 μm) of silicon assuming instant nucleation, for which the rate of silicon growth is given by Eq. (7). This figure shows that for high E_m (>0.6 eV), v_m increases monotonically with increasing laser power and T_p. (Note that the assumption of a steady-state temperature distribution during scan velocities $\gg 1$ mm/s may not be valid, see Sec. II B.) For lower E_m (~ 0.45 eV), v_m first increases with laser power and T_p, and then v_m approaches saturation or possibly decreases at higher powers for which $T_p > T_c$. The error bars indicate the uncertainty in determining the maximum scan velocity when $T_p > T_c$.

Furthermore, the v_m curves in Fig. 16 were computed for the center of the scanned line ($Y = 0$). For low E_m and high laser power, the peak temperature in the scan may exceed T_c at $Y = 0$ but may be lower than this critical temperature at the edges ($|Y| > 0$). When this occurs, deposition may initiate at the edges, leading to a double line of nuclei symmetrically displaced about $Y = 0$, with no nuclei at the center of the scan. This is analogous to the absence of nuclei at the center in static LLCVD when $T_p > T_c$, as depicted in Figs. 12 and 13. Furthermore, in analogy with the static LLCVD experimental observation of volcano or donutlike microstructures, thick double-ridge lines have been observed sometimes in scanning LLCVD.[57] As with static LLCVD, this unusual morphology most likely occurs because of reactant starvation or viscosity effects at $Y = 0$ in post-nucleation deposition and not because of this nucleation effect.

VI. CONCLUSIONS

A model of nucleation during low pressure LLCVD has been developed and applied to thin film deposition of silicon from SiH_4 onto strongly binding substrates such as silicon, and onto weakly binding substrates such as SiO_2 and Si_xN_y. The model includes the effect of laser-substrate heating, low pressure gas transport, heterogeneous decomposition chemistry, and single adatom and possible two-atom cluster surface dynamics. The simulation takes place over a 150×150 Å area at a uniform temperature. The incubation time prior to nucleation and the percent of surface coverage versus time are obtained as a function of the SiH_4 pressure, surface temperature, and silicon surface binding energy. By comparing the temperature of the simulation grid with that produced at the surface with a specific laser power and spot size, the nucleation characteristics over the laser irradiation region are obtained.

For static laser heating, the nucleation phase of thin film growth is shown to influence the initial thin film morphology strongly. For a given SiH_4 pressure and silicon substrate binding energy, a critical temperature T_c is obtained such that for a laser-induced peak surface temperature $T_p < T_c$, nucleation initiates in the center of the laser irradiation region of the surface, while for $T_p > T_c$, nucleation initiates at a location radially displaced from the center of the laser irradiation region forming an annulus deposit of material. Also, the constant competition between adatom desorption and adatom migration produces a large incubation period when $T_p > T_c$, and the initial cluster density decreases when moving radially inward from the location of initial nucleation to the center of the laser-heated region of the surface.

The addition of two-atom cluster migrations and desorptions to the dynamics of nucleation has been analyzed briefly. Also, the influence of surface nucleation sites on the nucleation phase of thin film growth was examined and found to increase T_c and thus eliminate the annulus nucleation morphology.

The results for static-laser heating have been extended to scanning-laser heating to gain a qualitative understanding of nucleation during microstructure generation. An estimate for the upper limit of the scan velocity at which nucleation would just barely occur was derived as a function of peak temperature (laser power) and adsorbate–substrate binding energy.

Even though the simulation results presented here have been obtained for silicon deposition from SiH_4, the general features of these results are valid for the deposition of other materials at low pressure where only heterogeneous decomposition need be considered. This includes low pressure pyrolytic deposition from other hydrides, the metal alkyls, metal carbonyls, and the halides.[5] To model the deposition of these other materials, the level of complexity in the dissociation chemistry might have to be increased to take into account the dynamics of intermediates and volatile products which may remain on the surface.

To simulate the nucleation phase of thin film growth during high pressure LLCVD, this model would have to be refined to include the possible effect of homogeneous, gas phase dissociation chemistry of the parent molecule. Also, both the diffusive and convective flow of parent molecules, intermediates, and volatile products, between the laser heated region of the surface and the bulk of the gas would have to be included to treat gas transport at high pressures properly.

Experimental work is currently underway to characterize the nucleation and early growth stages of thin film growth by visible laser-CVD of silicon from SiH_4 onto well prepared surfaces of c-Si, SiO_2, and Si_xN_y.[58]

ACKNOWLEDGMENTS

Work performed under the auspices of the U.S. Department of Energy by the Lawrence Livermore National Laboratory under Contract No. W-7405-ENG-48. One of the authors (IPH) wishes to acknowledge support by the Office of Naval Research.

APPENDIX A: LASER-INDUCED TEMPERATURE DISTRIBUTION

Here we assume a Gaussian laser is incident on a material system consisting of a silicon substrate with an optional thin film of either silicon dioxide (SiO_2) or silicon nitride (Si_xN_y) surrounded by air, selected as a representative gas. The steady-state thermal diffusion equation in cylindrical coordinates is given by

$$\frac{1}{r}\frac{\partial}{\partial r}\left\{rK[T(r,z)]\frac{\partial T(r,z)}{\partial r}\right\}+\frac{\partial}{\partial z}\left\{K[T(r,z)]\frac{\partial T(r,z)}{\partial z}\right\} + H(r,z) = 0\,, \tag{A1}$$

where T is the temperature, $K(T)$ is the thermal conductivity, and $H(r,z)$ is the external heat source due to the absorption of laser photons by the substrate and is given by

$$H(r,z) = \frac{2.79P[1 - R_{\text{refl}}(T)]\alpha(T)}{\pi S^2} e^{-(1.67r/S)^2} e^{-\int \alpha(T)dz}, \tag{A2}$$

where P is the laser power, S is the FWHM of the radial intensity distribution, $\alpha(T)^{-1}$ is the temperature-dependent-photon absorption depth, and $R_{\text{refl}}(T)$ is the reflectivity given by Eq. (A12) below. The spatial dependence of $H(r,z)$ is determined by the spatial profile of the incident laser intensity, the temperature dependence of the index of refraction, and the temperature dependence of the absorption depth in the absorbing substrate.

The thermal conductivity of silicon as a function of temperature can be represented by the equation

$$K_{\text{Si}} = 299/(T - 99)\,, \tag{A3}$$

where K_{Si} has the units of W/cm K and T is in Kelvin. Since the thermal conductivity of silicon decreases monotonically by a factor of 7 from $T = 300$ K to its melting temperature $T = 1690$ K, a nonlinear relationship exists between the incident laser power density and the induced peak surface temperature. A small increase in the incident power density will produce a faster-than-linear increase in the induced temperature. The data available for $\mathrm{Si}_x\mathrm{N}_y$ indicate that to within experimental error, the thermal conductivity is approximately constant over the temperature range of 300 K to the melting temperature of $\mathrm{Si}_x\mathrm{N}_y$ at 2173 K, 0.06 W/cm K.[59] The thermal conductivity of SiO_2 at room temperature is reported to be $K_{\mathrm{SiO}_2} = 0.014\ (\pm 0.004)$ W/cm K (Ref. 59) and increases with temperature to a value in the range ~0.020 W/cm K at 1883 K, the melting temperature of SiO_2. Though these values will be used here, it should be remembered that the thermal conductivity of SiO_2 depends strongly on how the oxide film is formed.

Because the SiO_2 and $\mathrm{Si}_x\mathrm{N}_y$ films are < 1000 Å in thickness they should not perturb the thermal properties of the silicon substrate substantially. Therefore, the thermal conductivity of the various overlaying thin films was set equal to the room temperature values given by

$$K_{\mathrm{Si}_x\mathrm{N}_y} = 0.06 \tag{A4}$$

and

$$K_{\mathrm{SiO}_2} = 0.014\,, \tag{A5}$$

where K has the units of W/cm K.

The thermal conductivity of air is represented by[60]

$$K_{\mathrm{air}} = 1.049\times 10^{-4} + 5.647\times 10^{-7}T, \tag{A6}$$

where K_{air} has the units of W/cm K and T is in Kelvin. Since the maximum thermal conductivity of air (1.0×10^{-3} W/cm K at the melting temperature of silicon) is much lower than that of Si, SiO_2 or $\mathrm{Si}_x\mathrm{N}_y$, the heat flow from the silicon or overlaying thin film to air is negligibly small. In fact, results show that the surface temperature of a 1000-Å SiO_2 layer decreases by only 2% when heat flow into the surrounding air (or any common buffer gas) is included. It should be noted that the thermal conductivity of air is to a good approximation independent of pressure as long as the gas can be treated in the diffusion limit. Thus the thermal effects caused by a surrounding gas can be neglected.

To be specific, in these simulations, the laser wavelength was chosen to be 514.5 nm from the argon ion laser. At 514.5 nm, SiO_2 and $\mathrm{Si}_x\mathrm{N}_y$ are transparent and laser photons are absorbed only in the silicon substrate. The absorption coefficient of silicon at this wavelength can be expressed analytically by[61,62]

$$\alpha(T) = 0.628e^{T/433}\,, \tag{A7}$$

where α has the units of $\mu\mathrm{m}^{-1}$. Since α increases monotonically from $1.2\,\mu\mathrm{m}^{-1}$ at 300 K to $\alpha = 31\,\mu\mathrm{m}^{-1}$ at 1690 K, the temperature increases faster than linearly with increasing laser intensity for micron-dimensional laser spot sizes. This further accounts for the faster-than-linear temperature rise versus intensity dependence in silicon.

The reflectivity of the incident laser radiation depends upon the index of refraction of the various materials. The values of the index of refraction of silicon,[63] SiO_2,[64] and $\mathrm{Si}_x\mathrm{N}_y$ (Ref. 64) are given by

$$n_{\mathrm{Si}} = 4.1 + 3.65\times 10^{-4}(T - 300) \quad (T < 1690\ \mathrm{K})\,, \tag{A8}$$

$$n_{\mathrm{SiO}_2} = 1.5\,, \tag{A9}$$

$$n_{\mathrm{Si}_3\mathrm{N}_4} = 2.05\,, \tag{A10}$$

where T is the temperature in Kelvin.

Since the thermal conductivity, the photon absorption depth, and the index of refraction of silicon vary dramatically over the temperature range of interest from 300 to 1690 K, Eq. (A1) is solved numerically[5] using the Gauss Seidel finite difference method. By considering the energy balance relation at each grid point, the following difference equation is obtained for $r > 0$,

$$T(r,z) = \frac{H(r,z) + T(r,z+1)[KZ(r,z)/(\Delta z)^2] + T(r,z-1)[KZ(r,z-1)/(\Delta z)^2]}{KZ(r,z)/(\Delta z)^2 + KZ(r,z-1)/(\Delta z)^2 + [KR(r,z)/(\Delta r)^2](1+\Delta r/2r) + [KR(r-1,z)/(\Delta r)^2](1+\Delta r/2r)}$$
$$+ \frac{T(r+1,z)[KR(r,z)/(\Delta r)^2](1+\Delta r/2r) + T(r-1,z)[KR(r-1,z)/(\Delta r)^2](1+\Delta r/2r)}{KZ(r,z)/(\Delta z)^2 + KZ(r,z-1)/(\Delta z)^2 + [KR(r,z)/(\Delta r)^2](1+\Delta r/2r) + [KR(r-1,z)/(\Delta r)^2](1+\Delta r/2r)}, \tag{A11}$$

where r and z refer to specific grid points, Δr and Δz refer to the distance between grid points in the radial direction and distance into the substrate, respectively, and $KR(r,z)$ and $KZ(r,z)$ are the thermal conductivities evaluated at the average temperature between grid points (r,z) and $(r+1,z)$, and grid points (r,z) and $(r,z+1)$, respectively.

The solution of the steady-state temperature is computed by iterating Eq. (A11) starting with the initial condition that the entire material system is at 300 K. During each iteration, the reflectivity R_{refl} of the silicon substrate covered with the thin film overlayer is first computed. The reflectivity is a function of temperature since it depends upon the silicon absorption coefficient and the index of refraction of silicon, both of which are temperature dependent. The reflectivity of the material system is computed using the multipass optics formula[65] so that thin film effects, such as antireflection for $h = \lambda/4n$, where h is the thin film thickness, are properly considered. The reflectivity R_{refl} is given by

$$R_{\mathrm{refl}} = \frac{r_{12}^2 + r_{23}^2 + 2r_{12}r_{23}\cos(2\beta - \delta)}{1 + r_{12}^2 r_{23}^2 + 2r_{12}r_{23}\cos(2\beta - \delta)}\,, \tag{A12}$$

where

$$r_{12}^2 = \left(\frac{n_{\mathrm{film}} - 1}{n_{\mathrm{film}} + 1}\right)^2, \tag{A13}$$

$$r_{23}^2=\frac{(n_{\rm Si}-n_{\rm film})^2+(\alpha\lambda/4\pi)^2}{(n_{\rm Si}+n_{\rm film})^2+(\alpha\lambda/4\pi)^2} \qquad \text{(A14)}$$

and

$$\beta=\frac{2\pi h n_{\rm film}}{\lambda}, \qquad \text{(A15)}$$

$$\delta=\arctan\left[\frac{2n_{\rm film}(\alpha\lambda/4\pi)}{n_{\rm film}^2-n_{\rm Si}^2-(\alpha\lambda/4\pi)^2}\right], \qquad \text{(A16)}$$

where λ is the wavelength.

Next, the absorption coefficient at each grid point in the silicon is computed from Eq. (A7). The laser intensity is then calculated halfway between grid points from the relation

$$I(z)=I(z-1)e^{-\alpha(T)\Delta z} \qquad \text{(A17)}$$

and the power absorbed is obtained by subtracting the intensity between adjacent points in the z direction. Thermal energy is assumed to be generated at the same location where the photons are absorbed. Any spread in the absorbed photon energy due to the mobility of photo-excited charge carriers is ignored. Finally the thermal conductivities KR and KZ defined above are assigned to each of the grid points from Eqs. (A3)–(A6).

Equation (A11) is iterated for approximately 10 000 times to reach the final temperature distribution. Two sets of differently spaced grid points are used in both the silicon and the air layer, while the thin film contains one set of grid points. This choice enables a decrease in the number of iterations needed for convergence. Final convergence is determined when the maximum temperature differential between 100 iterations does not exceed 0.01 K for any of the grid points. Dirichlet boundary conditions are used to force the temperature of 300 K at $r=|z|=\infty$. Calculations show that this boundary condition can be met at a distance corresponding to 75 μm away from the center of the beam, 75 μm into the bulk of the silicon, and 75 μm into the air layer.

Diffraction of the laser beam in the silicon substrate is neglected in this calculation. This is a valid approximation as long as the Rayleigh range is long compared to the distance the laser light travels into the silicon. The Rayleigh range Z_0 is given by

$$Z_0=\pi n_{\rm Si}S^2/1.39\lambda\,. \qquad \text{(A18)}$$

The shortest Rayleigh range will occur when S is a minimum, which corresponds to a value of $\sim\lambda$ for a diffraction limited beam. Thus for $\lambda=0.5145$ μm and $n_{\rm Si}=4.2$, the shortest Rayleigh range $Z_0=0.721\pi n_{\rm Si}\lambda\approx 5$ μm. Since Z_0 is significantly greater than the absorption depth ($\sim$0.8 μm) even for the worst case conditions, the effects of diffraction in the silicon can be safely ignored.

APPENDIX B: ENERGY BARRIER PER MIGRATION

For a migration from the central position of the subcube (0,0,0) to a corner position on the lower plane ($-1,-1,-1$), the migration barrier is given by

$$\begin{aligned}E_p=E_{a\text{-}a}\{&bs_1[\phi_{1,0,0,}+\phi_{0,1,0}+(\phi_{0,0,-1}+\phi_{0,-1,0}+\phi_{-1,0,0})f]\\&+bs_2(\phi_{1,-1,0}+\phi_{-1,1,0}+\phi_{1,1,0}+\phi_{0,-1,1}+\phi_{-1,0,1}+\phi_{1,0,1}+\phi_{0,1,1}+\phi_{1,0,-1}+\phi_{0,1,-1})\\&+bs_3(\phi_{1,1,1}+\phi_{-1,1,1}+\phi_{1,-1,1}+\phi_{-1,-1,1}+\phi_{1,-1,-1}+\phi_{-1,1,-1}+\phi_{1,1,-1})\}\,.\end{aligned} \qquad \text{(B1)}$$

The migration barrier from $(0,0,0)\rightarrow(0,-1,-1)$ is given by

$$\begin{aligned}E_p=E_{a\text{-}a}\{&bs_1[(\phi_{0,-1,0}+\phi_{0,0,-1,}+\phi_{-1,0,0}+\phi_{1,0,0})f+\phi_{0,1,0}]\\&+bs_2(\phi_{0,1,-1}+\phi_{-1,1,0}+\phi_{1,1,0}+\phi_{0,-1,1}+\phi_{-1,0,1}+\phi_{1,0,1}+\phi_{0,1,1})\\&+bs_3(\phi_{-1,1,-1}+\phi_{1,1,-1}+\phi_{1,1,1}+\phi_{-1,1,1}+\phi_{1,-1,1}+\phi_{-1,-1,1})\}\,.\end{aligned} \qquad \text{(B2)}$$

The migration barrier from $(0,0,0)\rightarrow(-1,-1,0)$ is given by

$$\begin{aligned}E_p=E_{a\text{-}x}\{&bs_1\phi_{0,0,-1}f+bs_2[\phi_{1,0,-1}+\phi_{0,1,-1}]+bs_3(\phi_{1,-1,-1}+\phi_{-1,1,-1}+\phi_{1,1,-1})\}\\&+E_{a\text{-}a}\{bs_1[\phi_{1,0,0}+\phi_{0,1,0}+(\phi_{0,-1,0}+\phi_{-1,0,0})f]+bs_2(\phi_{1,-1,0}+\phi_{-1,1,0}+\phi_{1,1,0}+\phi_{1,0,1}+\phi_{0,1,1})\\&+bs_3(\phi_{1,-1,1}+\phi_{-1,1,1}+\phi_{1,1,1})\}\,.\end{aligned} \qquad \text{(B3)}$$

The migration barrier from $(0,0,0)\rightarrow(0,-1,0)$ is given by

$$\begin{aligned}E_p=E_{a\text{-}x}\{&bs_1\phi_{0,0,-1}f+bs_2[\phi_{0,1,-1}+(\phi_{-1,0,-1}+\phi_{1,0,-1})f]+bs_3(\phi_{-1,1,-1}+\phi_{1,1,-1})\}\\&+E_{a\text{-}a}\{bs_1[\phi_{0,1,0}+(\phi_{-1,0,0}+\phi_{1,0,0})f]+bs_2[\phi_{-1,1,0}+\phi_{1,1,0}+\phi_{0,1,1}+(\phi_{-1,0,1}+\phi_{1,0,1})f]\\&+bs_3(\phi_{-1,1,1}+\phi_{1,1,1})\}\,.\end{aligned} \qquad \text{(B4)}$$

The migration barrier from $(0,0,0)\rightarrow(-1,-1,1)$ is given by

$$\begin{aligned}E_p=E_{a\text{-}x}[&bs_1\phi_{0,0,-1}+bs_2(\phi_{0,-1,-1}+\phi_{-1,0,-1}+\phi_{1,0,-1}+\phi_{0,1,-1})\\&+bs_3(\phi_{-1,-1,-1}+\phi_{1,-1,-1}+\phi_{-1,1,-1}+\phi_{1,1,-1})]\\&+E_{a\text{-}a}\{bs_1[\phi_{1,0,0}+\phi_{0,1,0}+(\phi_{0,-1,0}+\phi_{-1,0,0})f]+bs_2(\phi_{1,-1,0}+\phi_{-1,1,0}+\phi_{1,1,0}+\phi_{1,0,1}+\phi_{0,1,1})\\&+bs_3(\phi_{1,-1,1}+\phi_{-1,1,1}+\phi_{1,1,1})\}\,.\end{aligned} \qquad \text{(B5)}$$

The migration barrier from (0,0,0) → (0, − 1,1) is given by

$$\begin{aligned} E_p = {} & E_{a\text{-}x}\,[bs_1\phi_{0,0,-1} + bs_2(\phi_{0,-1,-1} + \phi_{-1,0,-1} + \phi_{1,0,-1} + \phi_{0,1,-1}) \\ & bs_3(\phi_{-1,-1,-1} + \phi_{1,-1,-1} + \phi_{-1,1,-1} + \phi_{1,1,-1})] + E_{a\text{-}a}\{bs_1[\phi_{0,1,0} + (\phi_{0,-1,0} + \phi_{0,0,1})f] \\ & + bs_2(\phi_{-1,1,0} + \phi_{1,1,0} + \phi_{0,1,1}) + bs_3(\phi_{-1,1,1} + \phi_{1,1,1})\}\,. \end{aligned} \tag{B6}$$

The migration barrier from (0,0,0) → (0,0, − 1) is given by

$$\begin{aligned} E_p = {} & E_{a\text{-}a}\{bs_1(\phi_{0,-1,0} + \phi_{-1,0,0} + \phi_{1,0,0} + \phi_{0,1,0})f \\ & + bs_2[\phi_{0,-1,1} + \phi_{-1,0,1} + \phi_{1,0,1} + \phi_{0,1,1} \\ & + (\phi_{-1,-1,0} + \phi_{1,-1,0} + \phi_{-1,1,0} + \phi_{1,1,0})f] \\ & + bs_3(\phi_{-1,-1,1} + \phi_{1,-1,1} + \phi_{-1,1,1} + \phi_{1,1,1})\} \end{aligned} \tag{B7}$$

The migration barrier from (0,0,0) → (0,0,1) is given by

$$\begin{aligned} E_p = {} & E_{a\text{-}x}\,[bs_1\phi_{0,0,-1} + bs_2(\phi_{-1,0,-1} + \phi_{1,0,-1} + \phi_{0,1,-1} + \phi_{0,-1,-1}) \\ & + bs_3(\phi_{-1,-1,-1} + \phi_{1,-1,-1} + \phi_{-1,1,-1} + \phi_{1,1,-1})] \\ & + E_{a\text{-}a}[bs_1(\phi_{-1,0,0} + \phi_{1,0,0} + \phi_{0,1,0} + \phi_{0,-1,0})f \\ & + bs_2(\phi_{-1,-1,0} + \phi_{-1,1,0} + \phi_{1,-1,0} + \phi_{1,1,0})f]\,. \end{aligned} \tag{B8}$$

$\phi_{x,y,z} = 0$ if the location (x,y,z) in the subcube is filled, and $\phi_{x,y,z} = 1$ if the location (x,y,z) in the subcube is empty. The location (x,y,z) is represented by either a 0 or a ± 1 (for each x, y, and z) and refers to the direction in the (x,y,z) relative to the center of the subcube. The quantities $bs_1 = 1$, bs_2 and bs_3 are the bond strength factors described in the text in Sec. III C and f is the factor which produces the desired ratio of migration to desorption energy for an adatom on a bare substrate surface. The quantity $E_{a\text{-}a}$ refers to the adsorbate-adsorbate bond strength, while $E_{a\text{-}x}$ refers to the adsorbate-surface binding energy ($E_{a\text{-}s}$) or to the adsorbate-adsorbate binding energy ($E_{a\text{-}a}$) depending on the location of the atom. The energy barrier heights for moves into the remaining 18 positions of the subcube are obtained by a suitable rotation of the subcube.

[1] *Photon, Beam, and Plasma Stimulated Chemical Processes at Surfaces*, edited by V. M. Donnelly, I. P. Herman, and M. Hirose (Materials Research Society, Pittsburgh, PA, 1987).

[2] R. M. Osgood and T. F. Deutsch, Science **227**, 709 (1985).

[3] D. J. Ehrlich and J. Y. Tsao, in *VLSI Electronics: Microstructure Science*, edited by N. Einspruch (Academic, New York, 1984), p. 129.

[4] I. P. Herman, *Chemical Physics*, edited by D. Bäuerle (Springer, Berlin, 1984), p. 396.

[5] I. P. Herman, in *Photochemical Materials Processing*, edited by K. G. Ibbs and R. M. Osgood (Cambridge University, MA, 1988), p. 61.

[6] J. Bloem and W. A. P. Claassen, Philips Tech. Rev. **41**, 60 (1983/84).

[7] J. A. Venables, G. D. T. Spiller, and M. Hanbücken, Rep. Prog. Phys. **47**, 399 (1984).

[8] W. A. P. Claassen and J. Bloem, J. Electrochem. Soc. **127**, 194 (1980).

[9] W. A. P. Claassen and J. Bloem, J. Electrochem. Soc. **127**, 1836 (1980).

[10] W. A. P. Claassen and J. Bloem, J. Electrochem. Soc. **128**, 1353 (1981).

[11] J. Bloem, J. Cryst. Growth **50**, 581 (1980).

[12] J. A. Joyce and R. R. Bradley, Philos. Mag. **14**, 289 (1966).

[13] G. R. Booker and J. A. Joyce, Philos. Mag. **14**, 301 (1966).

[14] J. A. Joyce, R. R. Bradley, and R. R. Booker, Philos. Mag. **15**, 1167 (1967).

[15] M. M. Oprysko and M. W. Beranek, J. Vac. Sci. Technol. B **5**, 496 (1987).

[16] I. P. Herman and F. Magnotta (personal communication).

[17] J. Y. Tsao and D. J. Ehrlich, Appl. Phys. Lett. **45**, 617 (1984).

[18] J. Y. Tsao and D. J. Ehrlich, J. Cryst. Growth **68**, 176 (1984).

[19] V. Baranauskas, C. I. Z. Mammana, R. E. Klinger, and J. E. Greene, Appl. Phys. Lett. **36**, 930 (1980).

[20] I. P. Herman, R. A. Hyde, B. M. McWilliams, A. H. Weisberg, and L. L. Wood, in *Laser Diagnostics and Photochemical Processing for Semiconductor Devices*, edited by R. M. Osgood, S. M. Brueck, and H. R. Schlossberg (North-Holland, New York, 1983), p. 9.

[21] S. D. Allen, J. A. Goldstone, J. P. Stone, and R. Y. Jan, J. Appl. Phys. **59**, 1653 (1986).

[22] D. C. Skouby and K. F. Jensen, J. Appl. Phys. **63**, 198 (1988).

[23] F. Petzoldt, K. Piglmayer, W. Kräuter, and D. Bäuerle, Appl. Phys. A **35**, 155 (1984).

[24] C. R. Moylan, T. H. Baum, and C. R. Jones, Appl. Phys. A **40**, 1 (1986).

[25] T. T. Kodas, T. H. Baum, and P. B. Comita, J. Appl. Phys. **62**, 281 (1987).

[26] I. P. Herman, F. Magnotta, and D. E. Kotecki, J. Vac. Sci. Technol. B **4**, 659 (1986).

[27] D. E. Kotecki and I. P. Herman, in *Photon, Beam, and Plasma Stimulated Chemical Processes at Surfaces*, edited by V. M. Donnelly, I. P. Herman, and M. Hirose (Materials Research Society, Pittsburgh, 1987), p. 65.

[28] M. E. Coltrin, R. J. Kee, and J. A. Miller, J. Electrochem. Soc. **131**, 425 (1984).

[29] M. E. Coltrin, R. J. Kee, and J. A. Miller, J. Electrochem. Soc. **133**, 1206 (1986).

[30] A. F. Bernhardt, B. M. McWilliams, F. Mitlitsky, and J. C. Whitehead, in *Photon, Beam, and Plasma Stimulated Chemical Processes at Surfaces*, edited by V. M. Donnelly, I. P. Herman, and M. Hirose (Materials Research Society, Pittsburgh, 1987), p. 633.

[31] M. Lax, J. Appl. Phys. **48**, 3919 (1977).

[32] J. E. Moody and R. H. Hendel, J. Appl. Phys. **53**, 4364 (1982).

[33] J. C. Whitehead, F. Mitlitsky, D. J. Ashkenas, A. F. Bernhardt, S. E. Farmwald, J. L. Kaschmitter, and B. M. McWilliams, Proc. SPIE **621**, 62 (1986).

[34] C. H. J. Van den Brekel and L. J. M. Dollen, J. Cryst. Growth **54**, 310 (1981).

[35] B. S. Meyerson and J. M. Jasinski, J. Appl. Phys. **61**, 785 (1987).

[36] R. Viswanathan, D. L. Thompson, and L. M. Raff, J. Chem. Phys. **80**, 4230 (1984).

[37] J. H. Purnell and R. Walsh, Chem. Phys. Lett. **110**, 330 (1984).

[38] D. J. Robbins and I. M. Young, Appl. Phys. Lett. **50**, 1575 (1987).

[39] H. E. O'Neal and M. A. Ring, Chem. Phys. Lett. **107**, 442 (1984).

[40] R. C. Farrow, J. Electrochem. Soc. **121**, 899 (1974).

[41] R. C. Henderson, J. Electrochem. Soc. **119**, 772 (1972).

[42] M. K. Farnaam and D. R. Olander, Surf. Sci. **145**, 390 (1984).

[43] R. J. Buss, P. Ho, W. G. Breiland, and M. E. Coltrin, J. Appl. Phys. **63**, 2808 (1988).

[44] J. Y. W. Seto, J. Electrochem. Soc. **122**, 701 (1985).

[45] F. F. Abraham and G. M. White, J. Appl. Phys. **41**, 1841 (1970).

[46] S. V. Ghaisas and A. Madhukar, Phys. Rev. Lett. **56**, 1066 (1986).

[47] G. H. Gilmer and J. Q. Broughton, J. Vac. Sci. Technol. B **1**, 298 (1983).

[48] D. Kashchiev, J. P. Van der Eerden, and C. Van Leeuwen, J. Cryst. Growth **40**, 47 (1977).

[49] A. I. Michaels, G. M. Pound, and F. F. Abraham, J. Appl. Phys. **45**, 9 (1974).

[50] R. A. Outlaw and J. H. Heinbockel, Thin Solid Films **108**, 79 (1983).

[51] J. P. Van der Eerden, C. Van Leeuwen, P. Bennema, W. L. Van der Kruk, and B. P. Veltman, J. Appl. Phys. **48**, 2124 (1977).

[52] J. Salik, J. Appl. Phys. **57**, 5018 (1985).

[53] B. Lewis and J. C. Anderson, *Nucleation and Growth of Thin Films* (Academic, New York, 1978).

[54] S. H. Garofalini and T. Halicioglu, Surf. Sci. **114**, 161 (1982).

[55] M. W. Chase, Jr., C. A. Davies, J. R. Downey, Jr., D. J. Frurip, R. A. McDonald, and A. N. Syverud, *JANAF Thermochemical Tables* (American Chemical Society and the American Institute of Physics for the National Bureau of Standards, New York, 1985).

[56] S. D. Allen, J. Appl. Phys. **52**, 6501 (1981).

[57] D. Bäuerle, in *Chemical Physics*, edited by D. Bäuerle (Springer, Berlin, 1984), p. 166.

[58] D. E. Kotecki and I. P. Herman, Mater. Res. Soc. Symp. Proc. **101**, 119 (1988).

[59] Y. S. Touloukian, R. W. Powell, C. Y. Ho, and P. G. Klemens, *Thermophysical Properties of Matter: Thermal Conductivity, Nonmetallic Solids* (IFI Plenum, New York, 1970), Vol. 2.

[60] *CRC Handbook of Chemistry and Physics*, 62nd ed., edited by R. C. Weast (Chemical Rubber, Boca Raton, 1981).

[61] G. E. Jellison and F. A. Modine, Appl. Phys. Lett. **41**, 180 (1982).

[62] G. E. Jellison and F. A. Modine, Oak Ridge National Laboratory Report No. TM-8002, (1982).

[63] D. F. Edwards, in *Handbook of Optical Constants of Solids*, edited by E. D. Palik (Academic, New York, 1985), p. 547.

[64] S. M. Sze, *Physics of Semiconductor Devices*, 2nd ed. (Wiley, New York, 1981).

[65] M. Born and E. Wolf, *Principles of Optics* (Pergamon, Oxford, 1980).